Investigating the uptake of nanoparticle-sourced iron by *Staphylococcus aureus*

J.J. van Heuckelum

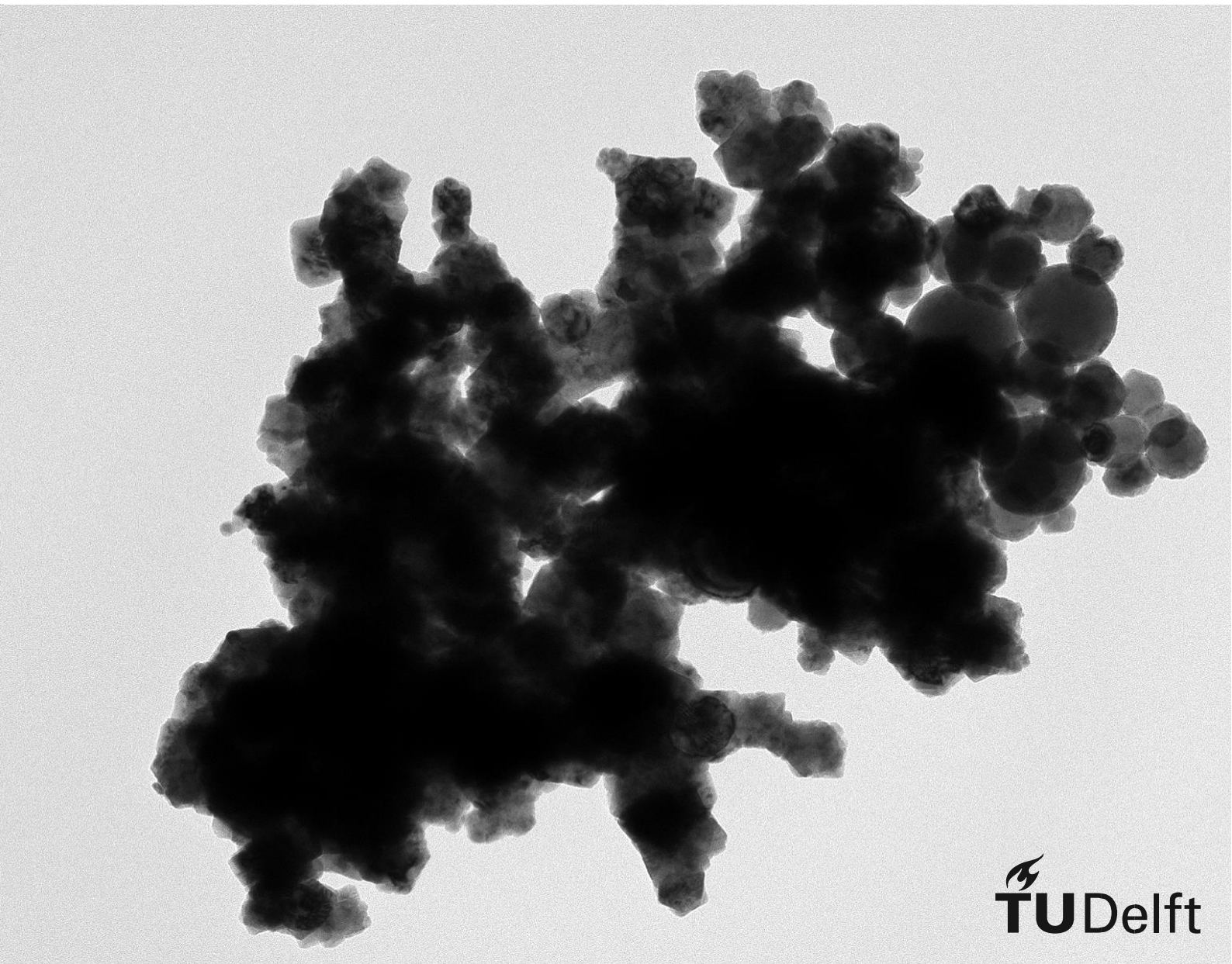

TU Delft

Investigating the uptake of nanoparticle-sourced iron by *Staphylococcus aureus*

By

J.J. van Heuckelum

in partial fulfilment of the requirements for the degree of

Master of Science
in Nanobiology

at the Delft University of Technology,
to be defended publicly on Friday December 15, 2023 at 10:00 AM.

Supervisors:	Dr. ir. R.M de Kruijff	TU Delft
	Dr. Peter-Leon Hagedoorn	TU Delft
	Dr. ir. I Apachitei	TU Delft
Thesis committee:	Dr. G. Bokinsky	TU Delft

TU Delft

Acknowledgements

I would first like to express my sincere gratitude to my supervisors Robin de Kruijff, Peter-Leon Hagedoorn and Iulian Apachitei, for their patience, wise counsel, valuable feedback and the weekly and monthly meetings. Though it has become cliché to write, this project would not have been there without them and I am deeply grateful to have been given the opportunity to work on it. I also want to thank Greg Bokinsky for taking the time to read this thesis and being on my thesis committee.

I want to thank both Baukje Terpstra and Astrid van den Meer for their invaluable help when I was working in the lab, from teaching me how to use the equipment in the laboratory to providing feedback when requested.
Additionally, I want to thank Eline van den Heuvel for the instruction and supervision when I first started with my radiation experiments, and instructing me how to measure samples with DLS. I would also like to thank Laura Koekkoek from the BOC group for teaching me how to grow and work with bacteria. I want to thank Robert Dankelmann for explaining XRD and doing the measurements, Gauri for performing TEM for me and Sietse Kuipers for instructing me how to use the Malvern Zetasizer. Without their help I would not have been able to acquire the valuable data necessary for further experiments.

Lastly, I want to thank the staff and students at the ARI group, including those who have already completed their projects, for the lunch and coffee. They made my time at the ARI group feel truly special. I especially want to thank Esther, for the great conversations and the exercise sessions we had. I am glad to have met you here.

Abstract

Implant associated infections by antibiotic-resistant biofilm-forming pathogenic bacteria such as *Staphylococcus aureus* have become a growing concern as they are difficult to treat and lead to implant revision surgery. Implant coatings consisting of superparamagnetic iron oxide nanoparticles may prevent the attachment to and infection of implants by bacteria. However, these nanoparticles release iron, which is also a nutrient necessary for bacterial growth, and may inadvertently contribute to infection. In this thesis the uptake of iron from iron nanoparticles by *S. aureus* is investigated.

To achieve this goal, nanoparticles were characterized, separation methods were developed and growth curves were constructed to determine the influence of nanoparticles on the growth of *S. aureus*. The release and uptake of iron from nanoparticles was investigated through the irradiation of iron nanoparticles and the measurement of the remaining ^{59}Fe after nanoparticle-supplemented growth.

It was found that only 3.7 ± 2.4% of nanoparticle iron was taken up by *S. aureus* after 24 hours, while 53 ± 12% of free iron was taken up. The percentage of iron that was taken up was found to be greater than the weight percentage of iron that was released from the nanoparticles.

While this demonstrates that iron remains with *S. aureus* after separation, it is not yet known whether this iron is truly internalized, or simply attached to the membrane. It also not conclusively known whether nanoparticle iron contributes to bacterial growth. Therefore, future experiments should be conducted to determine the internalization and the subcellular distribution of radioactive nanoparticle iron and its effects on bacterial metabolism.

Contents

Nomenclature

Acronyms and abbreviations

Acronym/abbreviation	Definition
S. aureus	*Staphylococcus aureus*
TKA	Total Knee Arthroplasties
THA	Total Hip Arthroplasties
PJI	Prosthetic Joint Infection
AMR	Antimicrobial Resistance
MRSA	Methicillin-Resistant *S. aureus*
PEO	Plasma-Electrolytic Oxidation
IONPs	Iron Oxide nanoparticles
ECM	Extracellular Matrix
AgNPs	Silver nanoparticles
FeNPs	Iron nanoparticles
DLS	Dynamic Light Scattering
XRD	X-ray Diffraction
TEM	Transmission Electron Microscopy
CCD	Charge-Coupled Device
DDD	Direct Detection Device
ICP-MS	Inductively Coupled Plasma Mass Spectrometry
ZnNPs	Zinc nanoparticles
PBS	Phosphate Buffered Saline
MWCO	Molecular Weight Cut-Off
BHI	Brain Heart Infusion
TSB	Tryptic Soy Broth
^{rad}FeNPs	Radioactive iron nanoparticles
EDL	Electrical Double Layer

Symbols

Symbol	Unit	Definition
OD_{600}	AU	Optical density at 600 nm
$OD_{600,\ max}$	AU	Maximum optical density at 600 nm
μ_{max}	h^{-1}	Maximum growth rate
t_i	h	Inflection time
$t_{1/2}$	s	Half-life
k_B	$m^2*kg*s^{-2}*K^{-1}$	Boltzmann constant, $k_B \approx 1.38 \times 10^{-23}\ m^2*kg*s^{-2}*K^{-1}$
T	K	Temperature
η	$N*s*m^{-2}$	Viscosity of a medium
R_H	m	Hydrodynamic radius of a particle
n	Dimensionless	Diffraction order
λ	nm	Wavelength
d	nm	Distance between layers of atoms
θ	°	Incident X-ray angle, Bragg angle
B	Dimensionless	FWHM of XRD peak
K	Dimensionless	Dimensionless shape factor
L	nm	Mean crystal domain size
m/z	$kg*C^{-1}$	Mass-to-charge ratio during Mass Spectrometry
F_{cor}	Dimensionless	Volume correction factor
v	$m*s^{-1}$	Sedimentation velocity of particle
d_c	m	Diameter of sphere
ΔP	$kg*m^{-3}$	Density difference between particle and medium
g	$m*s^{-2}$	Gravitational constant, $g = 9.81\ m*s^{-2}$

Biological and chemical glossary

Formula, symbol or name	Definition
MSCRAMM	Microbial surface recognizing adhesive matrix molecules, involved in *S. aureus* attachment to the ECM
ClfA	Clumping factor A, involved in *S. aureus* surface attachment
ClfB	Clumping factor B, involved in *S. aureus* surface attachment
fib	Fibrinogen-binding protein, involved in *S. aureus* surface attachment
PIA	Polysaccharide Intercellular Adhesin, involved in intercellular adhesion in *S. aureus* biofilm
PNAG	Poly-N-acetylglucomase, another name for PIA
ica	Gene locus that controls PIA production
IcaA	Protein responsible for PIA production
IcaB	Protein responsible for PIA deacetylation
IcaC	Protein responsible for PIA export
IcaD	Chaperone protein responsible for maintaining IcaA folding
Bap	Biofilm-associated protein
SasG	*S. aureus* surface protein G,
eDNA	Extracellular DNA, a component of *S. aureus* biofilm
QS	Quorum sensing, population density-dependent signalling system
Agr	Accessory gene regulator, the QS system of *S. aureus*
Rot	Toxin repressor downregulated upon Agr activation
PSM	Phenol-soluble modulins, lead to biofilm disruption
ROS	Reactive Oxygen Species, one of the primary antibacterial mechanisms of nanoparticles
ATP	Adenosine triphosphate, primary energy carrier in all living organisms
Ag^{+}	Silver ion

Formula, symbol or name	Definition
NADPH	Nicotinamide adenine dinucleotide phosphate, metabolic reducing agent and antioxidant responsible for ROS quenching
Fe_3O_4	Iron oxide, magnetite
Fe^{2+}	Iron ion
H_2O_2	Hydrogen peroxide
Fe^{3+}	Iron ion
Staphyloferrin A	One of the siderophores in *S. aureus* responsible for iron uptake
Staphyloferrin B	One of the siderophores in *S. aureus* responsible for iron uptake
NIS	NRPS-independent synthesis, responsible for staphyloferrin A and B production
Fur	Transcription factor that regulates staphyloferrin A and B synthesis and export
fur	Consensus sequence that Fur binds to
SfaA	Protein responsible for staphyloferrin A export
SbnD	Protein responsible for the export of staphyloferrin B
HtsABC	Protein responsible for staphyloferrin A-iron complex import
Sir	Staphylococcal iron regulated, system responsible for staphyloferrin B-iron complex import
Heme	Hemoglobin component used as an iron source by *S. aureus* during infection
Isd	Iron-responsive surface determinant, system that regulates *S. aureus* heme uptake
$AgNO_3$	Silver nitrate
HCl	Hydrogen chloride
HNO_3	Nitric acid
NaOH	Sodium hydroxide
Tris	Tris(hydroxymethyl)aminomethane, used as a buffer

1. Introduction

Medical implants can be used to replace worn out joints, repair bone and replace teeth, among other applications. They can improve quality of life and mobility for those suffering from osteo- and rheumatoid arthritis, reducing pain and injury. In 2019, in the United States alone, the number of Total Knee Arthroplasties (TKA) procedures approached half a million, while the number of Total Hip Arthroplasties (THA) procedures was more than a quarter million, an increase of 156% and 177% respectively compared to the year 2000 [1]. The annual volume of these operations is projected to increase greatly, with an increase of 176% for THA procedures and 139% for TKA procedures [1].

However, the use of these medical implants is not entirely risk-free. While mechanical failure and loosening are often found to be the most common reason for THA revision surgery, infection was also found to be significant cause of THA failure at approximately 10% [2,3]. Infection was found to be an even more common cause of THA revision failure, with infection being the reason for re-revision in approximately one-fifth of cases [4]. Additionally, infection was found to be the most common reason for TKA revision [5]. The incidence rate of implant-related infections varies based on the exact type of implant that is infected, with the incidence of Prosthetic Joint Infection (PJI) ranging between 1% and 2% [6,7], while the incidence of dental implant infection ranges from 2% to 3% [8]. Despite their low incidence rate, implant-related infections are a devastating complication, causing severe discomfort for the patient, leading to the above-mentioned revision surgery, and occasionally leading to fatal outcomes. The mortality rate for PJIs was reported to be 5.5% after one year and 7.3% after two years [9]. Implant-related infections also represent an economic burden, with PJIs costing $384,700,00 in the United States in 2017 alone, a number that is expected to more than double by 2030 due to the aforementioned increase of the annual volume of Total Joint Arthroplasties [10]. Because of the growing human and societal costs of implant-related infections it is important that more effective treatments and prevention strategies are developed.

Staphylococcus aureus (*S. aureus)* is a pathogenic bacterium found to be responsible for approximately a third of implant-related infections [11]. During infection, *S. aureus* adheres to the implant and then forms a biofilm, a community of bacteria encapsulated by an extracellular matrix produced by the bacteria [12]. The biofilm shields the bacteria from both the host immune system and antibiotics [13, 14], leading to more complicated treatment of implant infections. In recent decades, antimicrobial resistance (AMR) among bacteria has increased, with some estimates suggesting AMR will cause 10 million deaths per year in 2050 [15]. PJIs are no exception to the problem of AMR, as Methicillin-Resistant *S. aureus* (MRSA) has been reported to have been isolated in 45% of PJI cases [16]. The growth of AMR, combined with the fact that biofilms shield bacteria from antimicrobial drugs, has given rise to fears of virtually untreatable infections.

Because they are so difficult to treat and will likely become more difficult to treat in the future, it is important to prevent medical implant infections before they even happen. Common strategies to prevent medical implant infections include reduction of risk factors such as obesity and smoking, and antibiotic prophylaxis, the use of antibiotics to prevent infection [17]. Another strategy to prevent infection would be to prevent the attachment of bacteria by means of an antimicrobial surface on the implant.

A number of different approaches to such an antimicrobial surface exist, such as killing the bacteria upon contact, the release of antimicrobial agents, and surfaces that prevent bacteria from adhering to the implant [18]. Nanoparticles made from silver [19], copper oxide [20] and zinc oxide [21] have been demonstrated to possess antimicrobial and antibiofilm activity against *S. aureus*. These nanoparticles could be attached to the surface of an implant using the Plasma Electrolytic Oxidation process (PEO), and function as an antimicrobial surface [22]. The PEO process is a process where metal oxide coatings are generated by the application of a high electrical potential that results in dielectric breakdown followed by discharges and plasma reactions [23].

Iron oxide nanoparticles (IONPs) are another possible candidate for implant antimicrobial surfaces. They have been reported to exhibit antimicrobial activity against *S. aureus* and are capable of reducing biofilm growth, though it should be noted that they were not part of a surface in the cited study [24]. IONPs can also be superparamagnetic, which allows them to be heated by the application of an alternating magnetic field if he IONPs have a particular size [25]. IONP hyperthermia has been reported to reduce *S. aureus* biofilm viability, increase bacterial antibiotic susceptibility, and even augment macrophage bactericidal activity against intracellular bacteria [26]. The use of IONPs likely represents an effective method to prevent implant infections by antimicrobial-resistant bacteria, though more research is necessary to determine whether IONPs exhibit these same properties when incorporated onto a surface. However, IONPs also release iron [27], which is an important nutrient for bacterial growth. *S. aureus* has developed sophisticated mechanisms to acquire iron during an infection [28], and the bacterium could possibly take up iron released from nanoparticles. Iron is even implicated in *S. aureus* biofilm formation, with a reported increase in biofilm production and thickness when iron was supplied in the form of hemoglobin [29]. The addition of IONPs might therefore be counterproductive, as *S. aureus* could hypothetically use the iron released from the nanoparticles to augments its growth.

An effective method to investigate the uptake and subcellular distribution of iron by bacteria is to use a radioactive tracer. The medium used to grow bacteria is supplemented by a radioactive iron isotope, such as ^{55}Fe or ^{59}Fe, that acts as a radiotracer. By measuring the radioactivity after bacterial growth it is possible to determine the exact uptake of iron by the bacteria. This method has previously been used to study the metabolism of iron in mammals [30] and has also previously been applied in this research group to investigate the iron uptake of *S. aureus* under varying pH [31]. If the nanoparticles themselves are irradiated it may be possible to determine nanoparticle-released iron uptake.

This thesis therefore aims to investigate whether iron that is released by nanoparticles is taken up by *S. aureus* bacteria, using the radioactive isotope ^{59}Fe as a radiotracer. To this end, first several types of nanoparticles will be characterized by measuring their size, aggregation state, composition, surface potential and ion release. The effects of iron and silver nanoparticles on bacterial growth will be investigated. Thereafter, bacteria will be grown in the presence of radioactive iron nanoparticles in order to determine the uptake of iron by the bacterial cells.

2. Theoretical background

2.1 Implant-associated S. aureus infections

As mentioned previously, implant-associated infections are a devastating complication of implant surgery that are difficult to treat [2]. Implant-associated infections are classified into a number of categories, according to the route of infection and time until onset of infection symptoms after implantation surgery [32]. Perioperative infections refer to infections where bacteria enter the body during or immediately after surgery. During perioperative infections bacteria can originate from surgical equipment, clothing worn by the staff, the operating theatre or the patient themselves [32]. Up to 30% of the population is a carrier of *S. aureus*, where the nose is the most frequent site of colonization [33]. Nasal carriage is seen as the most important risk factor for surgical site infection in orthopedic surgery [34]. Screening and decolonization of *S. aureus* has been proven to reduce the number of surgical site infections in implantation surgery [35], but will never completely prevent implant infection due to the other sources of bacteria. Bacteria can also originate from the patient's blood, in which case the infection is referred to as hematogenous. Hematogenous infections can happen any time after implantation [32]. During implant infection, *S. aureus* forms a biofilm which allows it to evade both antibiotics and the immune system. The two most important steps of implant infection, adhesion and biofilm formation, are explained below.

2.1.1 Adhesion

The first step in implant infection is bacterial adhesion, as bacteria are unable to form the characteristic biofilm that protects them from the immune system and antibiotics without first adhering to the implant. Adhesion is thought to occur in two separate phases, which are described below.

In the first phase, bacteria are brought and adsorbed to the biomaterial surface by physical forces including van der Waals attraction, Brownian motion and electrostatic interactions [32]. The physical interactions during the first phase are classified into long-range and short-range interactions [32]. Long-range interactions act over separation distances longer than 50 nm, and are responsible for transporting the bacteria to the implant surface. Van der Waals interactions forces are thought to have the longest range, acting at distances up to 1 μm, and become stronger as bacteria move closer to the biomaterial surface [37]. Short-range interactions, which consist of chemical bonds, hydrophobic interactions and electrostatic interactions, can only occur when the separation distance is less than 5 nm [38]. The initial attachment of bacteria to the surface makes the second phase of adhesion possible [39].

The second phase of bacterial adhesion consists of specific molecular interactions between the bacteria and implant surface [32]. After implantation, implants are covered in proteins originating from the blood and interstitial fluid, including Extracellular Matrix (ECM) components [38]. *S. aureus* can generate adhesins referred to as microbial surface components recognizing adhesive matrix molecules (MSCRAMMs), which can bind to these ECM components [41]. Examples of MSCRAMMs responsible for surface attachment include Clumping factor A (ClfA), a 92 kDa protein, Clumping factor B (ClfB), a 124 kDa protein, and the fibrinogen-binding protein (fib), all of which bind to fibrinogen [41]. *S. aureus* can use MSCRAMMs to adhere to the implant surface and initiate infection.

During the first stages of infection, bacteria have to compete with tissue integration, a concept referred to as the 'race for the surface' [42]. If bacteria adhere to the surface first, it is more difficult for the implant to be properly integrated by the body [42]. It is therefore important to prevent bacteria from adhering to the biomaterial surface.

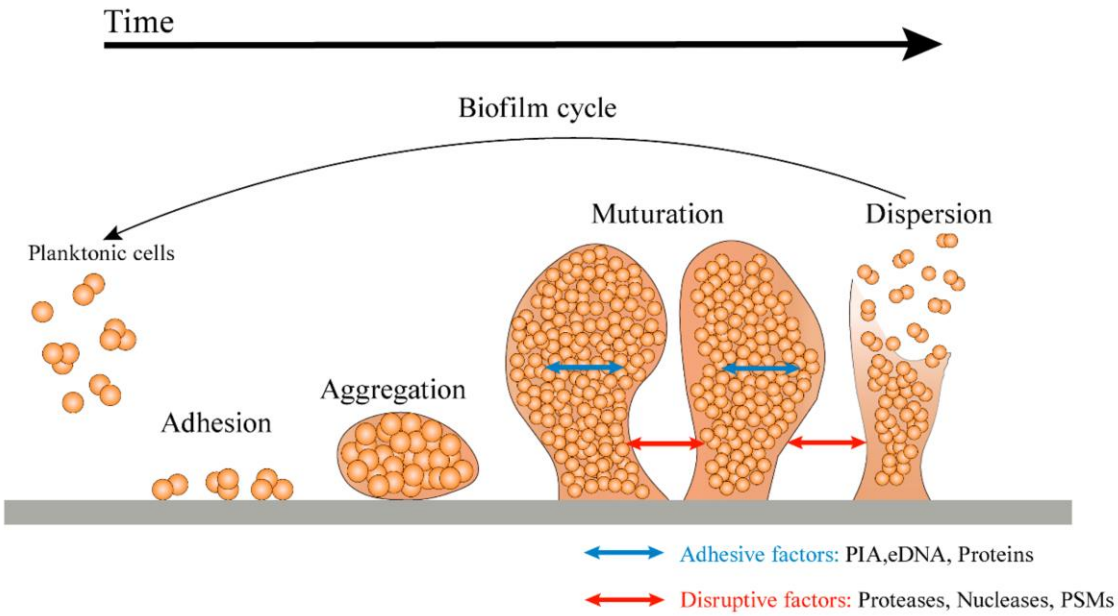

Figure 2.1: Biofilm formation during implant infection. After initial adhesion, bacteria begin to produce adhesive factors and aggregate, and form a biofilm. During maturation, disruptive factors are produced which give structure to the biofilm and eventually lead to its dispersion. Image taken from [36].

2.1.2 Biofilm formation and dispersal

After bacterial adhesion, bacteria such as *S. aureus* replicate, aggregate and begin to develop a biofilm. A biofilm is defined as a complex multicellular aggregate of bacteria encased in a self-produced extracellular matrix [43]. The biofilm formation process consists of four different steps: adhesion, aggregation, maturation and dispersion, displayed in figure 2.1 [36]. As adhesion has already been discussed previously, this section will only discuss the other three steps.

In the aggregation stage, bacteria proliferate and aggregate, and they begin to form an extracellular matrix that leads to the formation of microcolonies. Environmental signals also lead to the activation of regulatory networks, eventually giving rise to the formation of a biofilm [36].

During the maturation stage, a number of adhesive and disruptive processes take place that expand the biofilm and give it a complex structure [44]. Adhesive processes link bacteria together during replication, while disruptive processes form channels that are necessary to bring nutrients to bacteria in the deepest layers of the biofilm [44].

One of the most important molecules responsible for *S. aureus* adhesion in biofilm is known as Polysaccharide Intercellular Adhesin (PIA), often referred to as poly-N-acetylglucomase (PNAG) [45]. PIA is an exocellular polymer comprised of acetylglucosamine residues that is positively charged [45]. The positive charge of PIA is required for its role in intercellular adhesion [36]. The production and regulation of PIA are controlled by the *ica* locus, which consists of the *icaA, icaD, icaB* and *icaC* genes, and are displayed in figure 2.2 [44].

Of these genes, *icaA* and *icaD* are responsible for the production of PIA, where the icaA protein adds more N-acetylglucosamine residues to the PIA chain while icaD protein maintains the folding of icaA. *icaC* codes for a transmembrane protein likely responsible for transport of PIA to the cell surface, while the icaB protein deacetylates PIA, which gives it its positive charge [44].

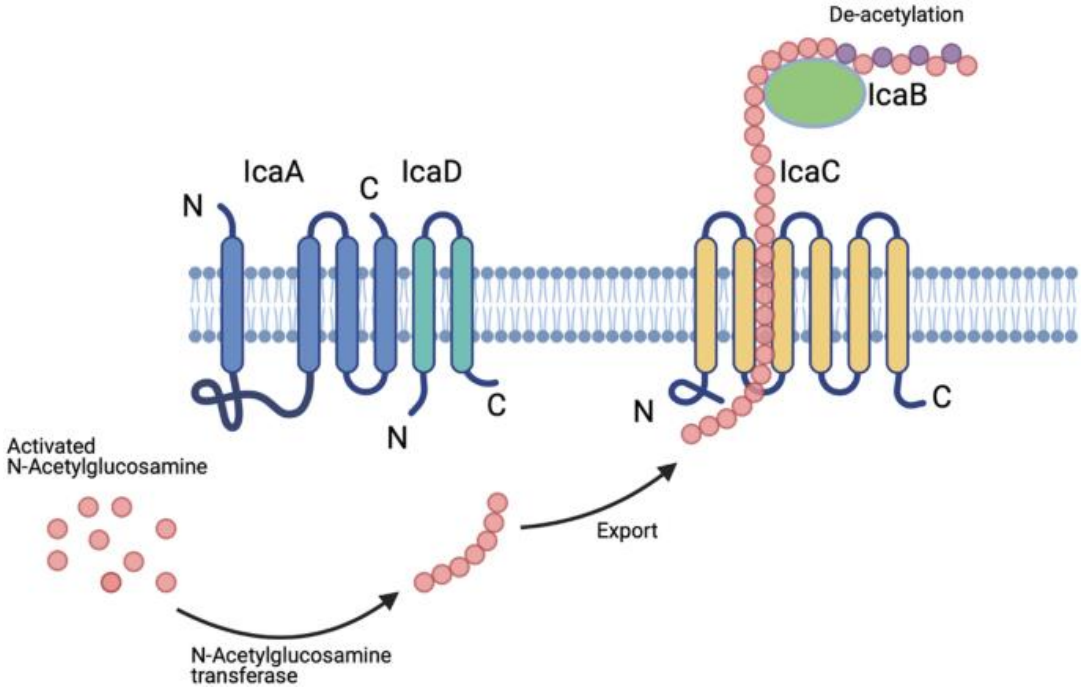

Figure 2.2: The production process of PIA. icaA (N-acetylglucosamine transferase) polymerizes the N-acetylglucosamine subunits while icaD acts as a chaperone protein. IcaC exports the polymer across the membrane, where icaB deacetylates PIA. Image adapted from [45]

PIA synthesis is not the only mechanism responsible for *S. aureus* biofilm formation, however, as a number of strains have been identified that are capable of biofilm formation while the *ica* locus is not present [47]. A number of proteins, including the Biofilm-associated protein (Bap), *S. aureus* surface protein G (SasG), and various fibronectin-binding proteins, have been observed to facilitate intercellular adhesion and biofilm formation [36]. Strains where the genes that are responsible for the production of these proteins were present have been reported to possess strong biofilm-forming ability [36]. Finally, a third mechanism of biofilm formation in *S. aureus* comes in the form of extracellular DNA (eDNA). The addition of nucleases to a biofilm can affect biofilm maturation, indicating that eDNA is a component of the *S. aureus* biofilm [48].
As mentioned previously, disruptive processes give structure to the biofilm, including the creation of channels responsible for nutrient transport. One mechanism responsible for the disruption and maturation of the biofilm is Quorum Sensing (QS) [44]. Quorum sensing is a type of cellular signalling where the expression of genes changes depending on the population density of surrounding bacterial cells. Bacteria release signal molecules known as autoinducers, that increase in concentration as cell density increases. Once a certain threshold is reached, bacteria alter their gene expression [49]. The quorum sensing system of *S. aureus* has been named Accessory gene regulator (Agr). Agr consists of a number of different signalling molecules and an effector molecule called RNAIII [44].

Activation of Agr leads to the reduction of the expression of surface adhesins, increases the production and secretion of extracellular proteases, and downregulates the expression of Rot, a toxin repressor [36]. Simultaneously, Agr activation also leads to the production of phenol-soluble modulins (PSMs), surfactant molecules which are responsible for the formation of channels necessary for nutrient transport in biofilms [50]. The increased production of proteases that break down protein molecules responsible for adhesion within the biofilm and production of PSMs responsible for channel formation lead to the structuring and maturation of the biofilm [36].
The final stage of the biofilm process is dispersion. As discussed previously, the production of PSMs and disruption of biofilm adhesion due to the production of proteases lead to the formation of channels in the biofilm. However, these two processes also lead to the dispersal of the biofilm, as bacterial cells are no longer adhered to one another. This allows bacterial cells to detach from the biofilm to spread to new niches within the body [50]. The dispersed bacteria can seed new sites of infection and cause sepsis [51].

2.1.3 Biofilm antibiotic resistance mechanisms

As discussed previously, bacteria within biofilms become more resistant to antibiotics [14]. A number of mechanisms are responsible for this antibiotic resistance. The first mechanism is resistance at the surface of the biofilm. Due to the complex structure of the biofilm, which consists of polysaccharides, extracellular DNA and proteins, antibiotics may be unable to penetrate the biofilm at all, or can only penetrate slowly as diffusion coefficients are lower than outside of the biofilm [14]. Slower diffusion of the antibiotic can also lead to deactivation before it can reach the bacterial target [52]. The second mechanism of biofilm antibiotic resistance is the microenvironment present deeper inside the biofilm. The bactericidal effects of antibiotics may be suboptimal in the biofilm microenvironment due to the presence of waste, metabolic byproducts, pH changes and low oxygen levels the antibiotics are not designed for [52]. Thirdly, a number of bacteria inside the biofilm can enter a state in which they become more resistant to stressful conditions such as the presence of antibiotics. These so-called persister cells do not divide until antibiotics are no longer present [52]. The antibiotic resistance of persister cells is caused by the shut-down of antibiotic targets [53]. Once the bacteria begin dividing again, they become susceptible to antibiotics again [52]. Because bacteria become resistant to antibiotic treatment once a biofilm has been formed, it is important to prevent implant infection rather than treat it.

2.2 Nanoparticle-based implant coatings

To prevent bacterial adhesion to and infection of medical implants, antimicrobial implant coatings may be developed. As previously discussed, three strategies exist to develop antimicrobial surfaces: contact-killing, adhesion prevention and antimicrobial agent release [18]. Metallic nanoparticles may be applied for the development of antimicrobial surfaces due to their ability to release toxic metallic ions and generate reactive oxygen species [54]. This section will discuss the efficacy and antimicrobial mechanism of the nanoparticles that are most relevant to this thesis, namely nanoparticles made of silver (AgNPs) and iron oxide.

2.2.1 Silver nanoparticle coatings

Silver has been known to possess antimicrobial properties for centuries [55]. Silver nanoparticles (AgNPs) have found numerous applications in the food industry and

healthcare, in particular in wound dressings, surgical mesh, and drug delivery [55,56]. AgNPs can also be immobilized, through processes such as the previously mentioned PEO, onto implants to function as an antimicrobial coating [22]. In this manner, AgNPs achieve high antimicrobial activity at lower doses than other nanoparticles, such as those made from copper or zinc, but they were also found to exhibit lower cytocompatibility [22]. The antimicrobial activity of silver nanoparticles is thought to originate from a number of different mechanisms, namely silver ion release and Reactive Oxygen Species (ROS) generation [22]. The different antibacterial mechanisms of AgNPs are displayed in figure 2.3. In general, released silver ions may disrupt the cell wall and membrane, denature ribosomes, interrupt ATP production and interfere with DNA replication. ROS can also disrupt the membrane. Free-floating AgNPs, which are unlikely to be present in the case of an antimicrobial implant coating, are capable of denaturing and perforating the cell membrane [56]. A recent study has confirmed many of these findings for *S. aureus* in particular [55]. It has been shown that the Ag^+ ions released by AgNPs target and bind to a number of different proteins in *S. aureus*. Ag^+ ions were found to primarily target proteins involved in the glycolysis, ROS defense and oxidative pentose phosphate pathways. The latter pathway is responsible for the production of precursors for nucleotide synthesis and NADPH, an important antioxidant responsible for ROS quenching [55]. It was therefore concluded that Ag^+ ions target the energy metabolism of *S. aureus*, while simultaneously disrupting oxidative stress defense systems, eventually leading to ROS accumulation and cell death. Because Ag^+ affects a number of different pathways at once, it is thought that cells are unable to develop resistance to Ag^+ [55]. The combination of silver and antibiotics was demonstrated to have a greater bactericidal effect than antibiotics alone, and was found to suppress the evolution of antibiotic-resistant bacteria [55]. Ag^+-releasing AgNPs are therefore thought to be a good alternative to antibiotics when combatting resistant bacteria such as MRSA.

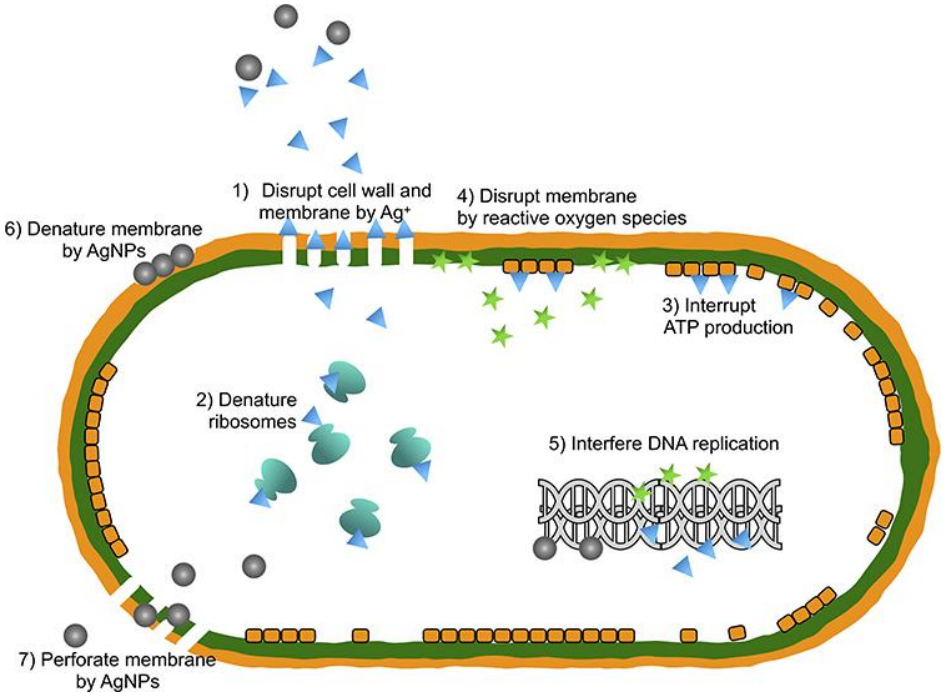

Figure 2.3: Mechanisms of the antibacterial action of AgNPs. Ag^+ ions can disrupt the cell wall, denature ribosomes, interrupt ATP production, interfere with DNA replication and release ROS that disrupt the membrane. AgNPs can also perforate and denature the bacterial membrane. Image taken from [56].

2.2.2 Iron oxide nanoparticle coatings

Like silver nanoparticles, nanoparticles made from Fe_3O_4 (IONPs) also possess antibacterial and anti-biofilm properties against *S. aureus* [24]. They can be used for a number of applications, including drug delivery, hyperthermia, and contrast enhancement for magnetic resonance imaging [57]. However, as they exhibit antibacterial activity, they may hypothetically be applied to develop an antimicrobial implant coating. Similarly to silver nanoparticles, the antibacterial mechanism of IONPs is thought to rely on ion release and ROS generation. Fe^{2+} ions released from IONPs may react with H_2O_2 to form ROS in the so-called Fenton reaction, which can damage the DNA, lipids and proteins [58]. Free-floating IONPs are also capable of binding to and damaging the cell wall [58]. This will be less important if the IONPs are incorporated into an implant coating.

As mentioned in chapter 1, Fe_3O_4 can also be superparamagnetic. Superparamagnetism is a type of magnetism that occurs in small particles such as IONPs. Because the particles are so small, individual particles are considered to have a single magnetic domain and therefore possess a single magnetic moment, which can flip randomly because of temperature. If observed for an amount of time much longer than the Néel relaxation time, the typical time it takes for the magnetic moment to flip, the average magnetization is measured to be zero [59]. When exposed to an magnetic field, particles either change their magnetic moment to align with the magnetic field while remaining stationary (Néel relaxation), or rotate themselves (Brownian relaxation). These processes can generate heat [60]. If exposed to an alternating magnetic field large amounts of heat can be generated that can be used for various applications, such as eradicating biofilms [26].

2.3 Staphylococcus aureus

S. aureus is a gram-positive bacterium that can be part of the microbiota, but can also cause diseases such as implant infection. Gram-positive bacteria such as *S. aureus* possess an envelope consisting of a thick layer of peptidoglycan, a mesh-like structure made of carbohydrate chains. Present inside this peptidoglycan layer are molecules called teichoic acids, which have a negative charge. The negative charge of the teichoic acids results in the negative surface charge of *S. aureus* [61].

2.3.1 *S. aureus* iron uptake mechanisms

In vertebrates, iron is ordinarily sequestered inside intracellular proteins, as it is highly reactive and potentially toxic. Therefore, *S. aureus* has developed a number of different strategies to acquire iron during infection [28]. One of the key strategies *S. aureus* uses to acquire iron is the production of siderophores. Siderophores are small secondary metabolites with a high affinity for ferric iron, Fe^{3+} [62]. *S. aureus* releases two different siderophores, staphyloferrin A and staphyloferrin B. While the two staphyloferrins are structurally different, it is unknown if each has a unique role during infection. The production of siderophores is performed by two different pathways in bacteria, which consist of non-ribosomal peptide synthesis (NRPS) and NRPS-independent synthesis (NIS). Both staphyloferrin A and B are produced through the NIS pathway [28]. The synthesis and export of both siderophores are regulated by the Ferric Uptake Regulator (Fur) protein, a transcription factor that bind to a consensus sequence called *fur* in the presence of iron. Fur functions as a repressor and prevents the infection of iron uptake genes when iron is present. If *S. aureus* does not have enough iron Fur releases from the DNA and transcription can begin [28]. Export of staphyloferrin A and B are

performed by SfaA and SbnD respectively. Outside of the cell, the siderophores form a complex with iron, which is then taken up by HtsABC for staphyloferrin A, and the Staphylococcal iron regulated (Sir) system for staphyloferrin B [62]. Once the siderophore-iron complexes have been internalized, iron needs to be recovered. Two different iron release mechanisms have been described, but little else is known. The first mechanism revolves around the reduction of Fe^{3+} to Fe^{2+}, which has a lower binding affinity. Due to the lower binding affinity iron is then released from the siderophore and can be bound to other proteins and stored. The second mechanism consists of the hydrolyzation of the siderophore, which results in the release of iron [62].
Another mechanisms by which *S. aureus* can acquire iron during infection is the uptake of heme. In the body heme is the precursor to hemoglobin, which used by the red blood cells to bind oxygen, and is the form in which most of the iron in the body is stored [28]. *S. aureus* might even prefer heme-iron over iron bound to transferrin, which is the primary source of iron stolen by siderophores [28, 62]. *S. aureus* is capable of secreting hemolysins, proteins that break open erythrocytes (red blood cells) to release hemoglobin, which the bacterium can then bind to in order to extract heme [62]. *S. aureus* heme uptake is regulated by the iron-responsive surface determinant (Isd) system, which transports captured heme through the cell wall and then liberates iron from heme in the cytoplasm [62]. Iron is one of the key growth-limiting nutrients during *S. aureus* infection and its iron acquisition mechanisms therefore represent a possible target for new therapies against *S. aureus* infection. It is currently not known whether nanoparticles could represent a significant source of iron for *S. aureus*.

2.3.2 Quantifying S. aureus growth behaviour

In order to determine the effect of nanoparticles on *S. aureus*, the growth of the bacterium has to be measured and quantified. This can be achieved by the measurement of the optical density of the bacteria at 600 nm, the OD_{600}, followed by the construction of a growth curve. A mathematical model can then be used to estimate a number of different growth parameters which quantify bacterial growth behaviour. One model that can be used to achieve this is the Logistic Model. The Logistic Model (eq. 1) is an appropriate method to model bacterial growth because the nutrients inside the culture medium are limited, and therefore the growth of bacteria in broth is self-limiting. There are three unknown growth parameters that characterize bacterial growth: the $OD_{600,max}$ represents the maximum OD_{600} and therefore the maximum density of the biomass of the bacterium; μ_{max} represents the highest growth rate; t_i is the inflection time which is the point in time where the curvature of the growth curve changes sign and the growth rate starts decreasing [63].

$$OD_{600} = \frac{OD_{600,max}}{(1+e^{-\mu_{max}(t-t_i)})} \quad \text{(eq. 1)}$$

2.4 Radiolabeling with iron

Radiolabeling is a technique whereby a radioactive nuclide is used to trace the path of a molecule or atom under investigation. By measuring the radiation generated through the decay of the radionuclide, it is possible to determine the mechanisms behind reactions or biological processes. It is therefore a good technique to determine the release of iron from nanoparticles and its uptake by bacteria. The two iron isotopes most suitable for this purpose are ^{55}Fe and ^{59}Fe, due to their suitable half-lives ($t_{1/2}$ = 2.7 years and $t_{1/2}$ = 44.45 days respectively), as the half-lives of the other isotopes are

either too short or too long [64]. In this study, both ^{55}Fe and ^{59}Fe are produced during irradiation of iron nanoparticles (FeNPs), but only ^{59}Fe is used as a tracer. ^{59}Fe is a radioactive nuclide that decays to ^{59}Co through β^- decay (the emission of an electron). The decay of ^{59}Fe results in the emission of an electron with a number of possible different energies, and the emission of gamma radiation where two energies, 1099 keV and 1291 keV make up more than 90% of the possible emitted energies [64]. Because ^{59}Fe also emits gamma radiation it can be detected using gamma counting. In contrast, ^{55}Fe decays through electron capture and only emits low-energy Auger electrons and low-energy x-rays, and can therefore only be detected using Liquid Scintillation Counting (LSC), which takes more time to prepare. Therefore, only ^{59}Fe will be used in this study.

2.5 Measuring devices

2.5.1 Dynamic light scattering

Dynamic Light Scattering (DLS) is a technique that can be used to determine the hydrodynamic radius of small particles in suspension. Light generated by a laser enters the sample and is then scattered in all directions, as a function of the size and shape of the particles in the sample. Brownian motion, the random motion of particles in a medium caused by the particle's collisions with solvent molecules, causes the scattering intensity to fluctuate over time. The scattered light separates into mutually destructive phases that cancel out, and mutually constructive phases that lead to a detectable signal, a phenomenon known as Doppler Broadening. The intensity fluctuation rate depends on the diffusion coefficient of the particle, which itself is a function of the (hydrodynamic) radius of the particle according to the Stokes-Einstein equation (eq.2). It should be noted that the Stokes-Einstein equation is only valid for spherical particles in a liquid with low Reynolds number. In eq.2, k_B refers to the Boltzmann constant, T to the temperature, η to the viscosity of the medium and R_H to the hydrodynamic radius of the particle.

$$D = \frac{k_B T}{6\pi\eta R_H} \quad \text{(eq.2)}$$

In a DLS setup, laser light is scattered by a sample. The scattered light is then measured by a detector, which is either placed at 90°, 173° or 158° (the last two are referred to as 'backscatter detection') compared to the laser. A digital autocorrelator then uses the signal generated by the detector to determine the rate of the intensity fluctuations, which can be used to calculate the diffusion constant and particle size distribution [65].

2.5.2 X-ray diffraction

X-Ray Diffraction (XRD) is a technique used to determine the phase composition and structure of samples in liquid, solid or powder form. X-rays are scattered by the atoms in a sample. Because the wavelength of the X-rays is in the same order of magnitude as the distance between the atoms in a sample, they constructively interfere. This phenomenon is called diffraction. Diffraction only occurs when the Bragg condition, as described by Bragg's law (eq.3) is satisfied. In Bragg's law, n refers to the diffraction order, λ to the wavelength of the incident X-rays (in nm), d to the distance between layers of atoms (in nm) and θ to the incident angle of the X-rays (in degrees).

$$n\lambda = 2dsin(\theta) \quad \text{eq. 3}$$

Because every crystal structure scatters X-rays slightly differently, they produce a unique pattern of different scattering intensity peaks that can be used to identify different materials present inside a sample [66].
When the crystals in a sample are small, such as a sample consisting of nanoparticles, the small size of the crystals leads to a broadening of the Bragg peak as described by the Scherrer equation (eq. 4). In the Scherrer equation B refers to the width of the peak at half of the peak's maximum intensity, λ to the wavelength of the incident X-rays (in nm), K is a dimensionless shape factor that depends on the shape of the crystallite, L to the mean size of the crystal domain (in nm) and θ refers to the Bragg angle (in degrees) [67].

$$B = \frac{K\lambda}{Lcos(\theta)} \quad \text{eq. 4}$$

2.5.3 Transmission Electron Microscopy

Transmission Electron Microscopy (TEM) is a technique that uses electrons to image objects at a significantly higher resolution than light microscopes. The higher resolution is achieved because the de Broglie wavelength of an electron is considerably smaller than the wavelength of light [68].
In TEM electrons are produced in an electron source, also referred to as an "electron gun". An electron source produces electrons either through thermionic emission, where high temperatures allow the electrons to overcome the work function and be emitted by the source, and field emission, whereby a strong electrostatic field causes emission of the electrons. The electrons are led through the vacuum of the electron microscope by a column of electromagnetic lenses and apertures, which serve to focus the beam, minimize distortions, and magnify the image after the electrons have passed through the sample. A vacuum is necessary to prevent interactions between the electrons and the atmosphere, which would result in distortion of the image [68].
A number of interactions can take place between the beam electrons and atoms in the sample. These interactions are classified into elastic scattering, where no energy transfer takes place between the incident electron and sample atoms, and inelastic scattering where energy transfer does take place. Scattered electrons carry information about the sample and therefore contribute to image formation [68].
Similarly to an optical microscope, image formation takes place through the interference between electron waves. When the electron waves are in phase, the interference is constructive and the amplitude is increased. If the electron waves are out of phase destructive interferences takes place and the amplitude is decreased [68].
There are two types of contrast formation in TEM: amplitude and phase contrast. Amplitude contrast is achieved by the removal of a number of electrons before the image plane. As electrons are absorbed by the sample or scattered at very high angles, contrast is formed. Phase contrast is generated as the phase of electrons is modulated through sample interaction. Both amplitude and phase contrast are present in most TEM images [69].
A detector present in the image plane detects electrons and creates an image. Charge-coupled devices (CCD) and Direction Detection Devices (DDD) are used to detect electrons automatically and in a digital format. In a CCD camera, electrons first encounter a scintillation layer. This scintillation layer translates electrons into photons,

which reduces the accuracy of the image. DDD cameras can detect electrons directly, which removes the blurring associated with CCD [68].
TEM can be used to image objects light microscopes are incapable of imaging, such as nanoparticles.

2.5.4 Zeta potential measurement

The zeta potential is the measure of the electric potential of a particle at the slipping plane, the interface between the fluid attached to the particle surface and the fluid the particle is suspended in. The zeta potential depends on the net charge of the particle and the ions attached to it. The stability of the particle suspension can be predicted by the zeta potential, where particles with a potential below -30 mV or above 30 mV will form stable colloidal suspensions. The zeta potential is therefore an important property to measure as it can explain the behaviour of nanoparticles in suspension [70]. The zeta potential can be measured through the use of electrophoretic light scattering. This is a technique whereby a rapidly alternating electric field is applied onto a dispersion of charged particles. The electric field causes the particles to move, where the particle velocity and direction depend on the zeta potential of the particle. Light from a laser is then scattered by the particles in the dispersion. As the particles are mobile, the frequency of the scattered light has shifted (Doppler shift), compared to the incident laser. The doppler shift is then determined by combining the scattered light with that of the original laser, and the particle velocity is calculated. The zeta potential can then be calculated from the particle velocity [71].

2.5.5 ICP mass spectrometry

Inductively Coupled Plasma Mass Spectrometry (ICP-MS) is a technique that can be used to accurately measure the levels of elements present in a fluid, even at very low concentrations. In ICP-MS an inductively coupled plasma, a plasma generated by inductive heating, is used to atomize and ionise the sample. The ions are then extracted from the plasma and guided to the mass analyzer. All mass analyzers are essentially filters that separate ions according to their mass-charge ratio *m/z*. A number of different mass analyzers exist, including quadrupole, magnetic sector and time-of-flight analyzers. After passing through the mass analyzer the ions arrive at the detector. The most common detector used for ICP-MS is an Electron Multiplier, whereby ions that hit the detector generate a cascade of electrons that can be detected as a ‘count’ [72].

2.5.6 Gamma counting

Gamma counting is used to measure the gamma radiation that results from radioactive decay and can therefore be used to measure the radioactivity of samples. Gamma counters are typically scintillation counters. When an ionizing particle hits the scintillating material inside the counter, it results in the excitation of an atom or electron. The de-excitation of the excited particle results in the creation of a number of low-energy photons. These low-energy photons are led to a photomultiplier tube, where the impact of the photons causes the emission of photoelectrons, which are accelerated towards the first dynode inside the tube. The collision of a photoelectron with the dynode results in the release of secondary photoelectrons that then collide with subsequent dynodes. At the anode of the photomultiplier tube the impact of a large number of secondary electrons results in the measurement of a pulse that is then registered as a ‘count’ [73].

3. Methodology

3.1 Materials

Product name	CAS number	Supplier
$AgNO_3$	7761-88-8	Thermo Fisher Scientific
Brain Heart Infusion Agar	-	Merck Sigma
Brain Heart Infusion Broth	-	Merck Sigma
Dulbecco's Phosphate buffered saline	-	Biowest
HCl	7647-01-0	VWR International
HNO_3	7697-37-2	Honeywell
HyperMag C (Iron oxide nanoparticles)	-	nanoTherics
Iron – nanopowder, 40-60 nm particle size, 99% trace metals basis	7439-89-6	Merck Sigma
Iron oxide (II, III), magnetic nanoparticles solution – 20 nm avg. part. size, 5 mg/ml in H_2O	1317-61-9	Merck Sigma
MilliQ	-	Ultrapure water system, Advantage A10, Merck
NaOH	1310-72-2	Merck Sigma
Silver colloidal, 65-75% Ag bases	7440-22-4	Merck Sigma
Tris	77-86-1	Merck Sigma
Zinc nanopowder	7440-66-6	Skyspring Nanomaterials

3.2 Characterization of nanoparticles

Nanoparticles were characterized to determine several different properties. Dynamic Light Scattering (DLS) was used to determine the hydrodynamic radius and aggregation state of the nanoparticles. The composition of the nanoparticles was determined by using X-Ray Diffraction (XRD). In order to determine the actual size and shape of the nanoparticles, Transmission Electron Microscopy (TEM) was performed. The zeta potential of the nanoparticles was measured with a Malvern Zetasizer. The cumulative ion release of the nanoparticles was measured through dialysis, gamma counting and ICP-MS.

3.2.1 Dynamic Light Scattering

Silver (AgNPs), iron (FeNPs) and zinc (ZnNPs) nanoparticles were suspended in MilliQ or Phosphate Buffered Saline (PBS) to create nanoparticle suspensions with a concentration of 1 mg/ml. The Fe_3O_4 nanoparticle (IONPs) suspension was diluted five times by adding 600 µl of NP suspension to 2.4 ml MilliQ or PBS to create a Fe_3O_4 nanoparticle suspension with a concentration of 1 mg/ml. The silver and Fe_3O_4 NP suspensions were diluted 125 times and the iron and zinc NP suspensions were diluted 25 times in total, corresponding to final concentrations of 8 µg/ml for silver and Fe_3O_4, and 0.04 mg/ml for iron and zinc. This was done in order to make the suspensions transparent.

2 ml of nanoparticle suspension was pipetted into a DLS tube. Samples were made in triplicate, and control samples were made with only PBS or MilliQ without nanoparticles. Samples were sonicated for 60 minutes at a frequency of 40 kHz in a Branson 5800 Ultrasonic cleaner in order to homogenize the nanoparticles prior to DLS measurements. The samples were measured three times. The DLS setup consisted of a JDS Uniphase 633 nm 35 mW laser, an ALV sp 125 s/w 93 goniometer, a Perkil Elmer photon counter. An ALV-5000/epp digital correlator and software were used to estimate the nanoparticle size. Scattering was measured at 90° for 30 seconds. DLS laser intensity was manually adjusted in order to keep the measured count rate between 100 and 150 kHz in order to obtain the most accurate results.

3.2.2 X-ray diffraction

Iron, silver or zinc nanoparticles were placed in the sample holder. The surface was carefully made level and all remaining nanoparticles were removed. X-ray diffraction measurements were performed using a Panalytical X'Pert Pro powder diffractometer. Diffraction measurements were performed between 5° and 45°, with a step size of 0.008°. The obtained diffractograms were compared to pre-existing reference data to determine the composition of the nanoparticle samples.

3.2.3 Transmission Electron Microscopy

Iron and silver nanoparticles were suspended in MilliQ to create a nanoparticle suspension with a concentration of 1 mg/ml. The nanoparticle suspensions were then diluted 100x. 50 µl of the nanoparticle suspension was drop-casted onto a carbon TEM grid (Formvar/- Carbon 200 mesh Copper, Electron Microscopy Sciences). The grid was air-dried at room temperature for approximately 12 hours. Following sample preparation TEM images were taken using JEOL JEM-1400Plus Electron Microscope at an acceleration voltage of 120 keV. The diameter of the nanoparticles was then measured with the line tool in the FIJI distribution of ImageJ [74].

3.2.4 Zeta potential measurement

Iron, silver and zinc nanoparticles were suspended in MilliQ to create a nanoparticle suspension with a concentration of 1 mg/ml. A 1 mg/ml suspension of Fe_3O_4 nanoparticles was created in the same manner as was described in section 3.2.1. Nanoparticle suspensions were diluted until the suspension was both colorless and transparent and no nanoparticle aggregations were visible. Silver and Fe_3O_4 suspensions were diluted 625 times, corresponding to a final concentration of 1.6 µg/ml. The iron and zinc NP suspensions were diluted 25 times, corresponding to a final concentration of 0.04 mg/ml. Prior to inserting the sample, the DTS 1070 capillary zeta cell used for measurements was washed twice using ethanol, after which it was washed with demi water, and subsequently washed with MilliQ. Samples were inserted into the capillary cell using a syringe. Zeta potential measurements were done through the use of a Malvern Zetasizer nano pro. The zeta potential was measured in triplicate. Prior to and following the zeta potential measurements, DLS measurements were performed in order to ensure that the zeta potential measurements did not change the size of the nanoparticles or lead to aggregation.

3.2.5 ICP-MS to measure metal ion content

In order to measure the concentration of metals in a sample ICP-MS was used. Prior to measurement of the samples a calibration line was made by measuring several different concentrations of silver or iron ions which were created by diluting a 1000 mg/L stock suspension. Samples were prepared by adding 9.9 ml of 1% HNO_3 to 0.1 ml of a sample. The sample concentrations were determined by comparing the mass intensities of the samples with those of the calibration curve.

3.2.6 Nanoparticle ion release

In order to determine the amount of ions released by metallic nanoparticles, dialysis of several different types of nanoparticles was performed. Prior to dialysis, a length of Visking dialysis tube with a Molecular Weight Cut-Off (MWCO) value of 12000-14000 kDa and a diameter of 21 mm was soaked in MilliQ for 30 minutes to remove the glycerol that is added as a humectant. According to the manufacturer, the pore size of this membrane is 24 Å, or 2.4 nm. Because the pore size of this membrane is much smaller than the nanoparticles used in this project, this membrane was chosen for the dialysis experiments. Dialysis was done in a Heraeus HERACell stationary incubator at 37°C.All dialysis experiments described in this section were performed in triplicate. The experiments that investigate the ion release of AgNPs and FeNPs are discussed in section 3.2.6.1 and section 3.2.6.2 respectively.

3.2.6.1 Dialysis of AgNPs

To measure the ion release of AgNPs, 20 ml of a 2.5 mg/ml AgNP suspension was pipetted into a dialysis tube that had been closed on one end with a knot. The dialysis tube was then closed on the other end using a plastic clip and suspended in a measuring cylinder filled with 80 ml MilliQ. Each day after the start of dialysis, a 0.1 ml sample was taken from the outside of the tube and diluted 100x. Silver content of the samples was then measured using ICP-MS as described in section 3.2.5. The wt% of the ion release was calculated afterwards by dividing the total mass of silver ions in the measuring cylinder (which was obtained by multiplying the measured concentration with the dilution and volume) with the total mass of silver calculated with the measured concentration of AgNPs added to the tube prior to dialysis.

3.2.6.2 Dialysis of FeNPs

FeNP ion release experiments were also conducted. FeNPs were suspended in PBS to create a suspension with a concentration of 20 mg/ml. 800 µl of this suspension was added to 200 µl of the 45 mg/ml radioactive FeNP stock solution created in section 3.5.1. Theoretically, the resulting partially radioactive FeNP suspension had a total concentration of 25 mg/ml. This suspension was then divided into 10 aliquots of 100 µl, the activity of which was measured with a Perkin Elmer 2480 Wizard2 3 inch Automatic Gamma Counter for five minutes. All aliquots were then transferred into the dialysis tube together with 9 ml of PBS. The dialysis tube was closed off with a clip and suspended in a measuring cylinder filled with 40 ml of PBS. 20 ml samples were taken frequently, up to 28 days after the start of dialysis. The sample was measured in the Wallac gamma counter for 15 minutes, after which the sample was transferred back to the dialysis setup. The measured count rate was divided by the total count rate of the FeNPs prior to immersion to obtain the wt% of the released ions.

3.3 Separation method characterization

To prepare for future experiments, a number of different methods to separate nanoparticles from the surrounding liquid were examined. This was primarily done to remove water from the Fe_3O_4 NP suspension in order to prepare it for future irradiation. The methods that were investigated were freeze-drying, desiccation and (ultra)-centrifugation, as well as the use of an oven to remove the remaining water. Centrifuge settings to separate all of the nanoparticles from suspension were also investigated, the method of which is explained in sections 3.3.4 and 3.3.5.

3.3.1 Freeze-drying

2 ml of 5mg/ml Fe_3O_4 nanoparticle suspension was frozen in a Frigon freezer at -47.5 °C for 48 hours. The frozen suspension was then covered with parafilm which was perforated with holes to provide an outlet for the evaporating water. The frozen suspension was then placed into a Kinetic MNL-036-A vacuum freeze dryer, where it was brought to a pressure of 30 mTorr (around 4 Pa) and left for 48 hours. The sample was then resuspended in 2 ml of water. 1 ml of the sample was taken and ultrasonicated as described in section 3.2.1. The particle size distribution of the resuspended nanoparticle samples was then determined using DLS. All measurements were done in triplicate.

3.3.2 Desiccation

1 ml of a Fe_3O_4 nanoparticle suspension with a concentration of 5 mg/ml was placed in a vacuum desiccator with silica gel. The desiccator was put under vacuum and was removed after 6 days. Samples were weighed before and after vacuum desiccation to determine the amount of water that was removed. After 6 days in the desiccator the sample was removed and resuspended in water.

To determine whether an oven would remove more water from the nanoparticles, the previously described experiment was repeated, but an additional step was added where the nanoparticle powder was placed in an oven at 100 °C for 1 hour.

After sample preparation, DLS was performed to determine particle size after nanoparticle separation.

3.3.3 Ultracentrifugation separation

In addition to the separation experiments involving desiccation and freeze-drying, ultracentrifugation experiments were performed to take IONPs out of suspension.

A 5 mg/ml Fe_3O_4 nanoparticle suspension was prepared by diluting a 10 mg/ml HyperMag C IONP suspension. This suspension was then transferred to a Quick-Seal tube, which was sealed through the use of a cordless soldering device. Spacers were placed on top of the tubes, after which they were placed in an Beckman-Coulter Optima Max-E ultracentrifuge. The IONP suspension was centrifuged at 100,000 x g for an hour. Afterwards, the sample was weighed and the supernatant was removed through a syringe. After removal of the supernatant the sample was allowed to dry in air for an hour. The remaining IONPs were then weighed again while still in the tube. The previously described experiment was repeated, but a step was added where the sample was placed in an oven for an hour at 100 °C. To determine whether the IONPs have aggregated after centrifuging, the samples were resuspended in MilliQ and DLS was performed to determine the particle size distribution.

3.3.4 Centrifugation

To determine whether nanoparticles could be removed from suspension to prepare for future experiments, centrifugation was used. 1 mg/ml nanoparticle suspensions were prepared by suspending silver, iron and zinc nanoparticles in MilliQ. The 5 mg/ml Fe_3O_4 nanoparticle suspension was diluted 5x to create a 1 mg/ml suspension. All nanoparticle suspensions were diluted 5x to create suspensions with a concentration of 200 µg/ml. Nanoparticle suspensions were then transferred into Eppendorf tubes and centrifuged at various speeds in a Heraeus Biofuge A centrifuge for 10 minutes. Sample supernatant was then transferred to DLS tubes and DLS was performed to determine the presence of nanoparticles after centrifugation.

3.3.5 Ultracentrifugation

Ultracentrifugation experiments were conducted to determine whether ultracentrifugation was a suitable method to remove nanoparticles from suspension. 200 µg/ml nanoparticle suspensions were prepared in the same manner as described in section 3.3.4. NP suspensions were transferred to 1.5 ml Quick-Seal ultracentrifugation tubes using a syringe. The Quick-Seal tubes were then prepared as described in section 3.3.3. Samples were centrifuged at speeds of 100,000 x g for an hour. The supernatant was carefully removed using a syringe and transferred into DLS tubes. DLS was performed to determine the presence of nanoparticles in supernatant after centrifugation.

3.4 Bacterial growth

3.4.1 Preparation of culture media

In this project, Brain Heart Infusion (BHI) media were used to grow bacteria. BHI was chosen over Tryptic Soy Broth (TSB), another culture medium suitable for fastidious bacteria such as *S. aureus*, because it had been used for similar experiments within this group, and because research has shown that BHI was more suitable for biofilm formation than TSB [75]. While no experiments with biofilms are done in this thesis, future research will likely focus on biofilm formation and prevention. BHI broth was prepared according to the instructions of the manufacturer. 37 g of BHI broth powder was dissolved in 1000 ml of MilliQ water. pH measurements were performed to ensure the pH of the medium was at pH 7.4. The medium was then autoclaved at 121 °C for 15 minutes and placed in a fridge for storage.

BHI agar was used to prepare plate cultures. 26 g of BHI agar powder was dissolved in 1000 ml of MilliQ. The BHI agar was then sterilized through autoclave at 121 °C for 15 minutes. The agar was left to cool down for 30 minutes. Plates were poured by transferring 30 ml of agar into a Petri dish using a serological pipette. The plates were then allowed to solidify for 20 minutes, and left to dry in the biosafety cabinet for 30 minutes. The plates were then stored in a fridge at 4°C.

3.4.2 Preparation of *S. aureus* plate cultures

To reduce exposure to and prevent contamination of the RN0450 *S. aureus* stock, plate cultures were prepared. The use of agar plate cultures also allowed for the use of single colonies for inoculation. To prepare plates, BHI agar plates were streaked with liquid culture prepared using the stock or other plates. The plates were incubated at 37°C in a Heraeus HeraCell stationary incubator for 18 hours under a normal atmosphere. After preparation, the plates were stored at 5°C.

3.4.3 Preparation of liquid cultures

For bacterial growth experiments, a preculture was prepared the day prior to an experiment. A single colony of plated *S. aureus* was used to inoculate 50 ml of BHI broth in a 250 ml glass round-bottom flask. It was grown for 18 hours at a temperature of 37°C in a New Brunswick Scientific C24 Incubator Shaker at 155 rpm. To determine the dilution factor necessary to inoculate the media for experiments, optical density measurements at 600 nm (OD_{600}) were taken. Growth experiments were conducted in 250 ml to which 250 µl of preculture was added to 50 ml of BHI broth (a dilution factor of 200x). OD_{600} measurements were taken through the use of an UV-6300 PC spectrophotometer to verify inoculation. After inoculation bacteria were grown at 155 rpm and 37 °C in an orbital shaker.

3.4.4 Growth curve experiments

To determine the effect of the presence of nanoparticles on the growth of bacteria, growth curve experiments were performed. Bacterial cultures inoculated as described in section 3.4.3 were supplemented with 1 ml of water containing 0, 2.5 or 25 mg of iron or silver nanoparticles, to create bacterial cultures with a concentration of 0, 50 and 500 µg/ml respectively (hereafter referred to as ‘A’, ‘B’ or ‘C’). The culture flasks were then put in the orbital shaker for a period of 0-25 hours. To construct a growth curve, samples were taken at a number of time points between 0 and 25 hours after inoculation. To take a sample, 2 ml of bacterial culture was transferred to a disposable 4 ml acrylic cuvette using a pipette. Optical density measurements were then taken at 600 nm using the spectrophotometer. Samples were compared to reference samples that were prepared by suspending the corresponding amount of nanoparticles in BHI broth. The three growth parameters were estimated through the use of the Levenberg-Marquardt algorithm of the nonlinear curve fit tool in the OriginPro 2022 program.

3.5 Iron release and uptake

3.5.1 Production of radioactive iron nanoparticles

To create the radioactive iron nanoparticles (^{rad}FeNPs) used for ion release and iron uptake experiments, 100 mg of FeNPs was sealed in a quartz tube and irradiated for 100 h in the SmallBeBe-L (thermal neutron flux of $4.24 * 10^{17}$ s^{-1} m^{-2}) of the 2.3 MW Hoger Onderwijs Reactor (HOR) at the TU Delft Reactor Institute. It was calculated that an irradiation period of 100 hours and a cooling period of 48 hours would result in an activity of 10.6 MBq for ^{59}Fe. After a cooling period of 48 hours, the quartz tube was opened, and the nanoparticles were suspended in 200 µl of water and transferred to a separate plastic 15 ml tube, hereafter referred to as the stock solution. This was repeated until as many nanoparticles as possible were removed from the quartz tube. The stock solution was then filled up with water until the volume reached 10 ml.
This process was later repeated, but the stock solution was then filled up to 2 ml of volume instead. It was assumed that 90% of nanoparticles were removed from the quartz tube. Therefore, the two created stock solutions were considered to have a concentration of 9 mg/ml and 4.5 mg/ml.

3.5.2 Determining volume correction factors

The Perkin Elmer 2480 Wizard2 3 inch Automatic Gamma Counter used to measure samples in this study is sensitive to the geometry, including the volume, of samples measured.

To determine the factors necessary to correct for this effect, 0.1 ml of a radioactive source in the form of nanoparticles or ions created by dissolving nanoparticles in HCl was pipetted into a 20 ml glass vial or 1.5 ml Eppendorf tube. The activity was then measured in the Wallac gamma counter for five minutes. The sample volume was then increased by adding water (in steps of 2 ml for the glass vial and 0.2 ml for the Eppendorf tube) and new measurements were performed. This was then repeated until the sample container was full. The slope of the obtained graph was used to calculate the volume correction factors. The following equation (eq. 5) was used to calculate what the activity would be in a different volume than when it was measured.

$$A_y = A_x(1 - F_{cor})^{y-x} \quad \text{eq. 5}$$

Where A_y and A_x refer to the activity of a sample (in cpm) measured at their respective volumes y and x (in ml), while F_{cor} is the correction factor.

3.5.3 Bacterial nanoparticle iron uptake

FeNPs suspended in PBS were added to nanoparticles from the radioactive stock suspension to create a suspension with a concentration of 25 mg/ml. The activity of the created suspension was then measured in the Wallac gamma counter for 15 minutes. 1 ml of this suspension was added to a bacterial culture inoculated as described in section 3.4.3. The culture was grown for 18 hours at 37°C and 155 rpm. OD_{600} measurements were performed to verify and measure bacterial growth. After overnight growth the bacterial culture was transferred to a plastic 50 ml tube by serological pipette. The culture was allowed to settle for an hour at 5°C in a fridge in to allow the largest nanoparticle aggregates to sink to the bottom. The top 40 ml of the culture was transferred to a different 50 ml tube and centrifuged for 5 minutes at 90 x g. The supernatant was transferred to another 50 ml tube and centrifuged for 10 minutes at 4000 rpm and 5°C. The supernatant was removed and the pellet was resuspended in 10 ml 50 mM Tris-HCl (pH 8). The previous centrifugation and resuspension step was repeated. The created bacterial suspension was transferred to a glass 20 ml counting vial and its activity was measured in the Wallac gamma counter. Nanoparticle iron uptake experiments were performed nine times in total. The applied separation protocol was based on research by a previous student in the same group [31].

3.5.4 Bacterial iron ion uptake

70.5 mg of FeNPs was added to 100 µl of the radioactive nanoparticle stock suspension. The combined suspension was then dissolved in 2.7 ml of 1M HCl. 14 µl of 1M NaOH was then carefully added to the solution to increase the pH to approximately 4.0. 0.3 ml MQ was then added to the iron ion solution. 1 ml of the radioactive iron solution was added to a bacterial culture inoculated as described in section 3.4.3. The culture was grown for 18 hours at 37°C. OD600 measurements were performed after overnight growth. The bacterial culture was then transferred to a plastic 50 ml tube and centrifuged for 10 minutes at 4000 RPM and 5°C. The supernatant was removed and the pellet resuspended in 10 ml 50 mM Tris-HCl. The previous step was repeated. After the second round of centrifugation and resuspension the bacterial suspension was transferred to a 20 ml glass counting vial and its activity was measured in the Wallac gamma counter for 15 minutes. The ion uptake experiments were performed nine times in total.

4. Results and discussion

4.1 Nanoparticle characterization

4.1.1 Dynamic Light Scattering

DLS was performed to determine the size distribution and aggregation of AgNPs, FeNPs, IONPs and ZnNPs. The obtained size distribution peaks can be found in table 4.1. Size distribution figures resulting from DLS measurement can be found in Appendix A.

	MQ (nm)	PBS (nm)
AgNP	65.6	14.9
FeNP	114.5, 638.0	138.7, 848.1
IONP	27.2, 114.5	641.8
ZnNP	209.4, 1404.7	201.1, 1480.5

Table 4.1: Peaks of the size distribution of nanoparticles in nm

The DLS experiments suggest that the AgNPs and IONPs possess a smaller hydrodynamic radius than either FeNPs or ZnNPs. According to TEM data (discussed in section 4.1.3), the AgNPs were smaller than the FeNPs. According to manufacturer specifications, the IONPs possess a diameter of 20 nm and the ZnNPs a diameter of 60-80 nm. While the FeNPs and ZnNPs are therefore larger than the AgNPs and IONPs, their larger hydrodynamic radius can also be ascribed to aggregation of nanoparticles. This is consistent with visual observation of suspensions of FeNP or ZnNP, which were observed to be very unstable and aggregate and sediment within minutes after suspension. However, it should be noted that large particles scatter laser light more than small particles [76]. Therefore, a larger intensity peak in a size distribution figure may not necessarily mean that more particles of that size are present. One must also keep in mind that unstable suspensions sediment. Therefore, the DLS laser may unable to reach the largest nanoparticle aggregations, and their hydrodynamic radius can not be measured.

Another notable trend is that the hydrodynamic radius of nanoparticles (with the exception of AgNP) tends to increase when suspended in PBS, as can be seen in both Table 4.1 and figure A.1 in Appendix A. The observed increase may be explained by the adsorption of an electrical double layer (EDL) onto the surface. The EDL consists of a layer of ions – the Stern layer – with opposite charge to that of the particle and a layer of ions and counterions that grows on the Stern layer. If the concentration of ions is increased, such as in PBS, the double layer is compressed and the zeta potential decreases. The decrease of the zeta potential may lead to a lessening of particle stability, aggregation and a subsequent increase of the hydrodynamic radius [70, 71]. The increase of the hydrodynamic radius is observed to be greatest in case of the IONPs.

Lastly, one must remember that DLS measurements are snapshots of a specific group of particles (namely those that scatter laser light) at a specific point in time, and therefore may (and often will) vary between samples and measurements. The results presented in this section are therefore to be interpreted as such. In particularly stable suspensions, such as the AgNP suspension, this effect is fairly limited, but in more

unstable suspensions greater differences can be seen between measurements (Figure A.2, Appendix A). It is therefore difficult to establish a mean hydrodynamic radius and standard deviation of the nanoparticles, unless they are exceptionally stable.

4.1.2 X-Ray Diffraction

The composition of AgNPs, FeNPs and ZnNPs was determined with XRD. The obtained XRD data was compared to reference data obtained from the International Centre for Diffraction Data [77, 78, 79, 80]. The measured XRD patterns and reference data for all investigated nanoparticles are displayed in figure 4.1, 4.2 and 4.3. Tables with reference peaks that were compared to the obtained XRD patterns are displayed in appendix C.

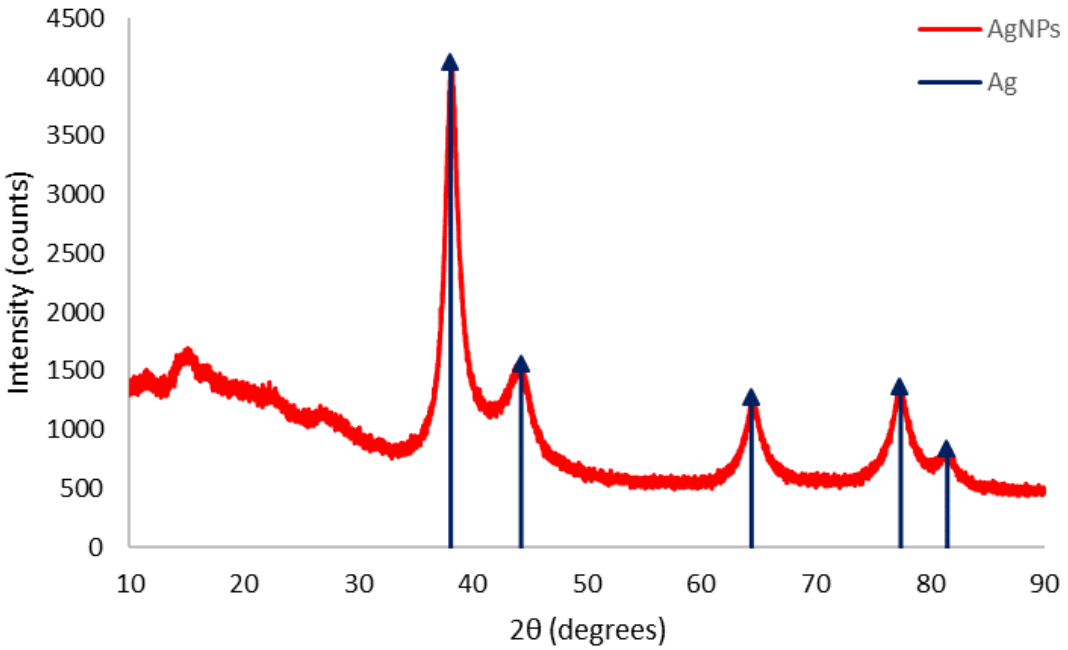

Figure 4.1: Obtained AgNP diffraction pattern (red) and reference XRD data for silver (blue)

The obtained XRD data for AgNPs is displayed in figure 4.1. It was determined that the XRD pattern of the AgNPs matched the reference data with reference code 00-004-0783, which is the XRD pattern for silver [77]. Small quantities of AgO may be present, but no significant amounts were detected. The broadening of the peak, which results from the small size of the AgNPs studied with XRD and which is explained in section 2.5.2, can also be observed in figure 4.1. This peak broadening appears to have no effect on the identification of the XRD pattern.

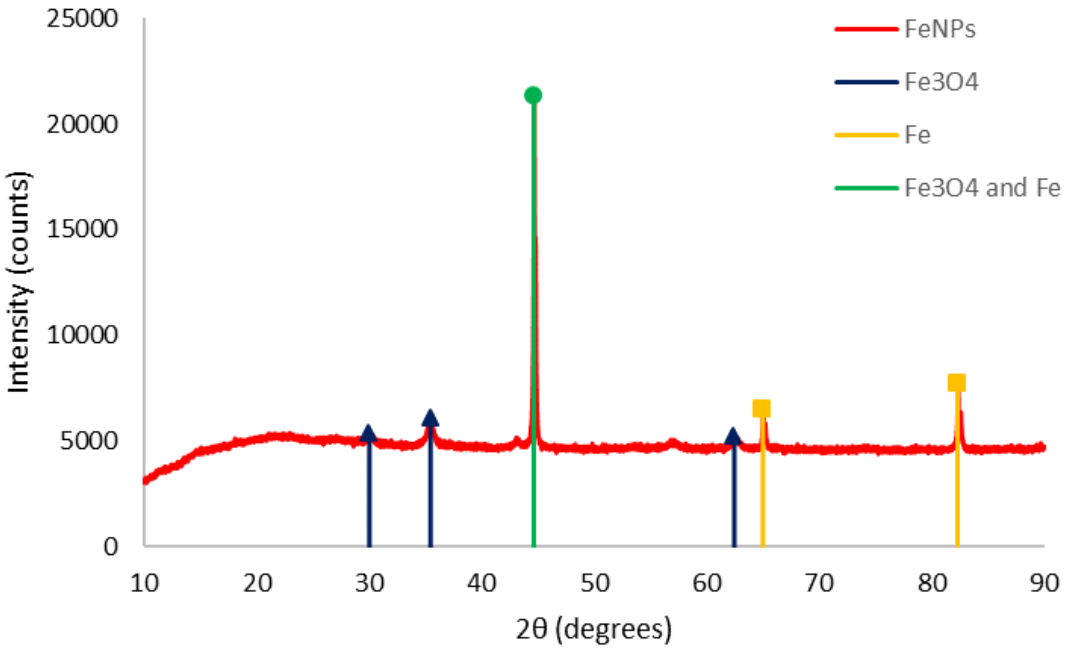

Figure 4.2: Obtained FeNP XRD pattern (red) and reference data for Fe_3O_4 (blue) and iron (yellow) [78, 79]. Peaks present in both reference data sets are displayed in green.

The obtained XRD pattern for FeNPs is displayed in figure 4.2. It has been determined that the XRD pattern of FeNPs matched the reference data for both Fe and Fe_3O_4 [78, 79]. This indicates that oxidation of the FeNPs has taken place. The intensity of an XRD diffraction peak in a multiphase sample is proportional to the fraction of the phase corresponding to that peak [81]. The peaks corresponding to the Fe_3O_4 reference data only are smaller than those corresponding to the Fe data, indicating that the oxidation of the nanoparticles is limited.
For example, the peak at position 35.479°, which would normally be the largest peak if XRD was performed on pure Fe_3O_4, has a total count rate that is more than three times smaller than the count rate of the peak at position 44.463°, the largest peak for Fe. The 44.463° peak is also obtained when Fe_3O_4 is measured, but has a much lower intensity than if it were measured in a sample consisting of iron, as indicated in the reference data in Appendix C. If the background is accounted for, this difference increases dramatically. Unlike with the AgNPs, no significant peak broadening was observed. As peak broadening is caused by a small crystal size, this is likely the result of the larger size of the FeNPs.

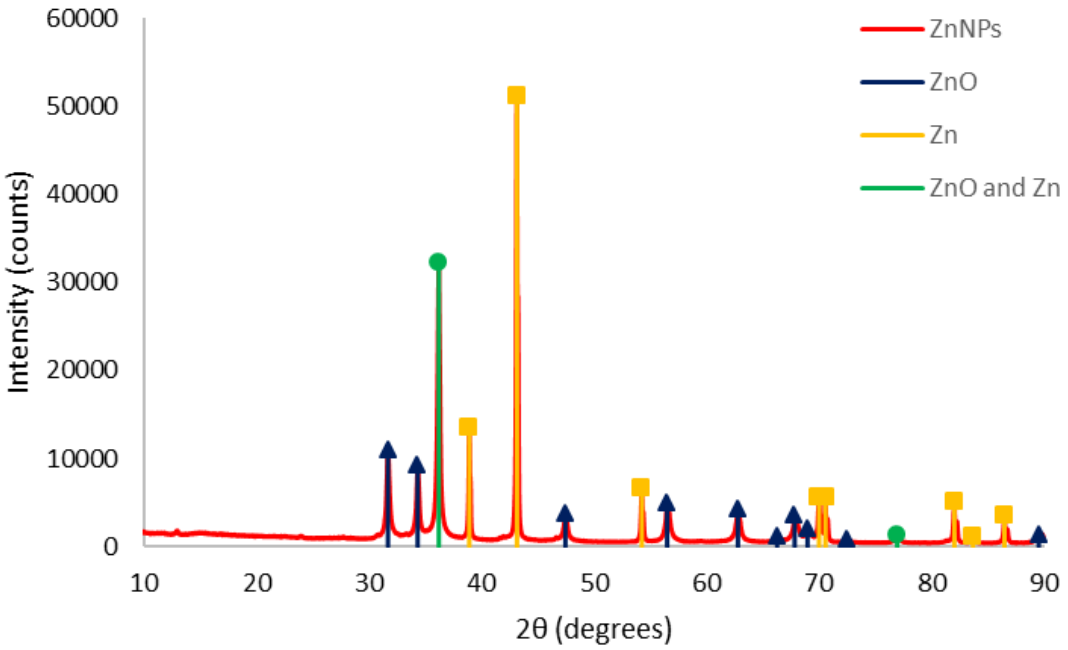

Figure 4.3: ZnNP XRD pattern (red), ZnO reference data (blue) and Zn reference data (yellow). Peaks present in both reference datasets are displayed in green.

The obtained XRD pattern for ZnNPs is displayed in figure 4.3. The XRD pattern of ZnNPs matches both the reference data for Zn and ZnO [77, 80]. As was the case for the FeNPs, oxidation of the ZnNPs has taken place. Contrary to the FeNPs, the degree of oxidation appears to be greater, as indicated by higher peaks at positions that indicate the presence of ZnO. This may indicate greater reactivity of the zinc nanoparticles. Similarly to the FeNPs, no peak broadening was observed as a result of the larger nanoparticle size used.

4.1.3 Transmission Electron Microscopy

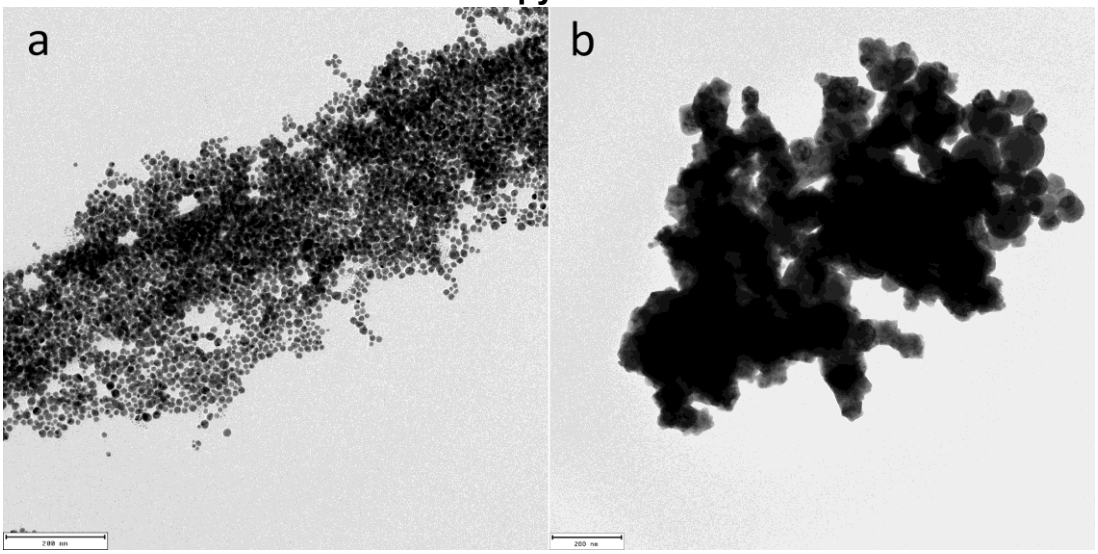

Figure 4.4: TEM images of AgNPs (a) and FeNPs (b).

In order to determine the size and the shape of the nanoparticles used in this project, TEM was performed on both the AgNPs and FeNPs. The diameter of the nanoparticles

was measured with ImageJ [74]. As can be seen in figure 4.4a, the AgNPs were observed to form large clusters, but many individual nanoparticles could be seen and were measured. The AgNPs were found to be spherical, and had an average diameter of 13.6 ± 3.3 nm. A number of AgNPs with a diameter an order of magnitude smaller than the average were also observed, as can be seen in figure 4.4a. The overall size distribution of the AgNPs closely matches the Weibull distribution centered around the average AgNP diameter, as can be observed in figure A.3a in Appendix A.
The FeNPs were also observed to aggregate, as can be seen in figure 4.4b, but individual nanoparticles were difficult to discern. Because FeNPs were more difficult to distinguish and therefore the diameter proved more difficult to measure, the total number of measured FeNPs (n = 97) is lower than the number of measured AgNPs (n = 220). The average diameter of FeNPs was found to be 73.8 ± 27.6 nm. A great variety of sizes was observed, as displayed in figure A.3b in Appendix A. A number of non-spherical shapes were also observed, displayed in figure A.4 in Appendix A, but it is not clear whether these are genuinely non-spherical nanoparticles, TEM artefacts or an aggregation of spherical nanoparticles projected onto an image.

4.1.4 Zeta potential

To obtain a greater understanding of the observed stability of the nanoparticles, the zeta potential was measured. The peak of the zeta potential was determined and is displayed in table 4.2. Figures of the zeta potential measured for each nanoparticle can be found in appendix A.

	Zeta potential (mV)
AgNP	-41.4 ± 1.3
FeNP	-33.0 ± 2.8
IONP	-28.6 ± 1.9
ZnNP	-29.9 ± 3.2

Table 4.2: Peaks of the zeta potentials of different nanoparticles in mV

The zeta potential for every nanoparticle was measured to be close to or below -30 mV, as can be seen in table 4.2. As described in section 2.5.4, these findings predict that suspensions made from any of these nanoparticles would be stable. However, this was observed not to be the case, as mentioned in section 4.1.1. When the zeta potential is measured, a bias may be introduced by the sedimentation of the investigated particles [82], as particles with zeta potentials that would be classified as unstable sediment and can no longer be measured. The FeNPs and ZnNPs were observed to sediment, as mentioned previously. It is therefore likely that the measured zeta potentials of both FeNPs and ZnNPs are biased towards particles with highly negative zeta potentials. While it may be possible to overcome this challenge by removing the DLS step prior to zeta potential measurement that was mentioned in section 3.2.4, as it reduces the time nanoparticles have to settle before they are measured, nanoparticles can still aggregate during the sample preparation step.
While the IONPs have the lowest zeta potential of all studied nanoparticles, they were observed to form one of the most stable suspensions, as only AgNP suspensions were more stable. The observed stability of the IONP suspension could also be ascribed to steric repulsion between nanoparticles, whereby a surfactant on the nanoparticle physically prevents the aggregation of nanoparticles. It was not known whether such as surfactant was present on the Sigma-Aldrich IONPs, but according to the

manufacturer the HyperMagC IONPs possess a meso-2,3-dimercaptosuccinic acid (DMSA) surfactant coating.

4.1.5 Nanoparticle ion release

To investigate the ion release of AgNPs and FeNPs, dialysis was performed. Because *S. aureus* can take up iron ions, and metal ions also exhibit antimicrobial activity, the ion release is an important property to study. In this section, the cumulative nanoparticle ion release is expressed as the percentage of the total weight of the nanoparticles. The findings of the dialysis experiments of AgNPs and FeNPs are discussed in section 4.1.5.1 and 4.1.5.2 respectively.

4.1.5.1 AgNP ion release

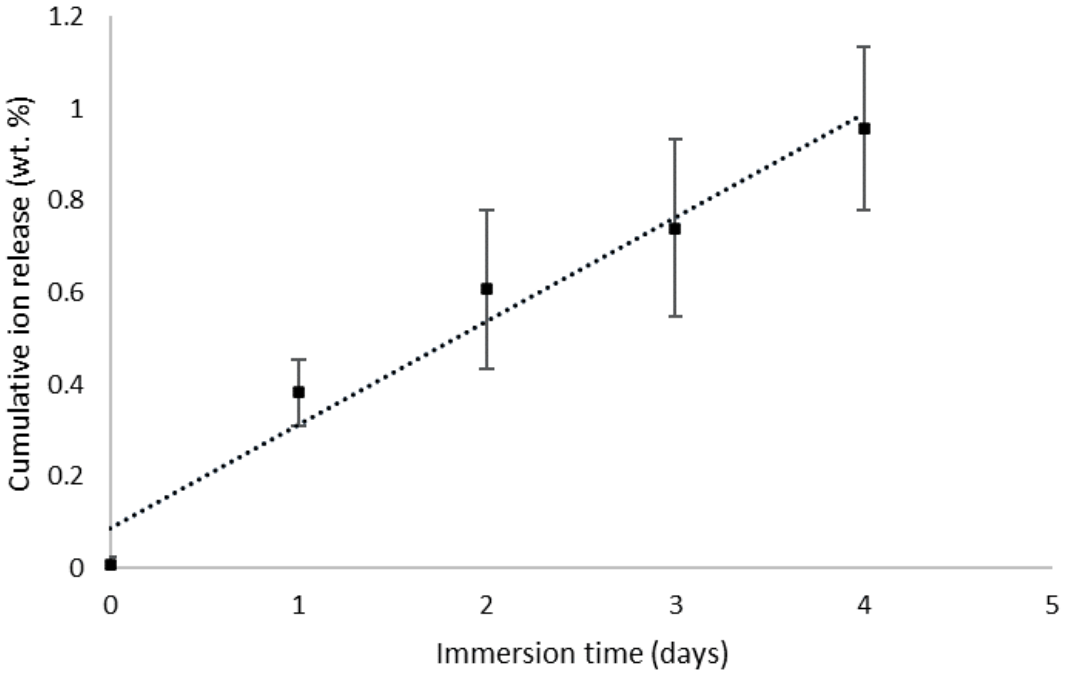

Figure 4.6: Cumulative silver ion release over time from AgNPs, expressed as the weight percentage of the total amount of silver inside the dialysis tube. The error bars indicate one standard deviation from the mean.

The mean cumulative silver ion release by AgNPs over time has been determined through ICP-MS, and is displayed in figure 4.6. The AgNP concentration added to the tube prior to immersion was measured to be 1.77 mg/ml, which is lower than the 2.5 mg/ml described in 3.2.6.1 that was actually put into the dialysis tube.
The cumulative ion release over time appears to follow a linear trend. A linear trendline fitted to the graph had an R^2 value of 0.9671, indicating a good fit. This trendline suggests a linear increase of the wt% of released silver ions with 0.23% per day. However, a number of different studies have shown that AgNP ion release shows an initial increase, only to gradually plateau over time until no more ions are released [83, 84]. If this experiment were to be repeated over a longer period of time, a similar ion release profile may be found.
It must also be noted that dialysis was performed in MQ at 37 °C. Nanoparticle ion release rates are influenced by the pH, temperature particle size and the presence of surfactants among other factors [83]. If experiments are performed in a different

medium, such as the BHI broth used later in this thesis, the ion release will likely be different.

4.1.5.2 FeNP ion release

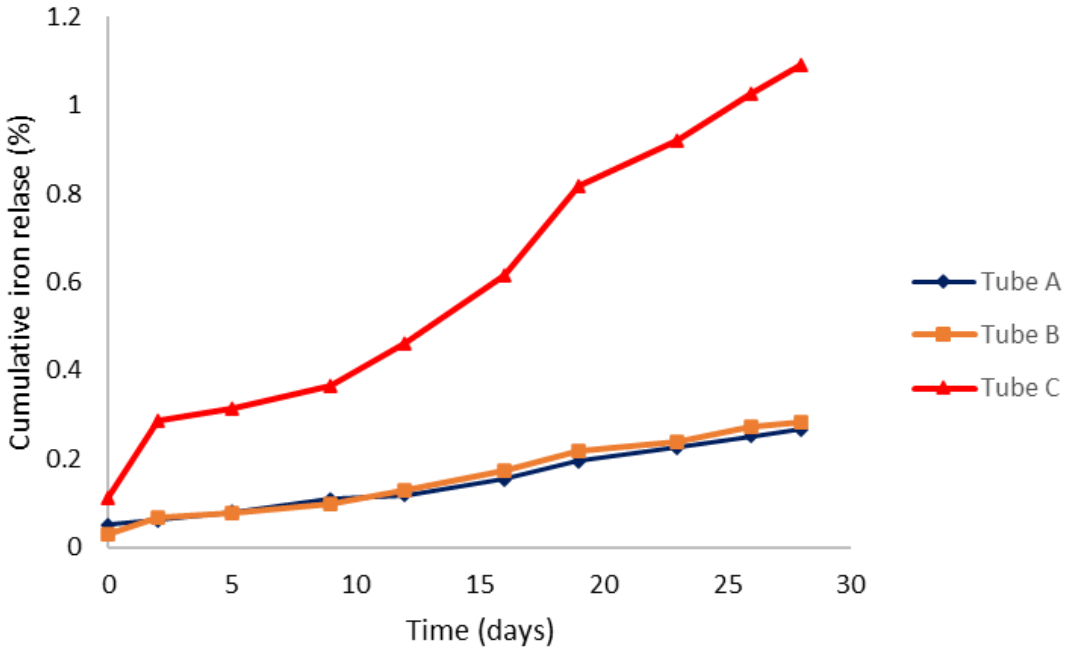

Figure 4.7: Cumulative ion release of FeNPs in PBS. Different dots represent different dialysis tubes.

The mean cumulative ion release of FeNPs in PBS was determined by measuring the count rate of samples outside of the dialysis tube. The obtained findings from the FeNP dialysis experiment are displayed in figure 4.7. Because the FeNPs tend to aggregate and sediment, the nanoparticle suspension is unstable. As mentioned in the previous section, this may lead to uneven pipetting, whereby the concentration of a pipetted sample is different than that of the sample it came from. When taking radioactive FeNPs from the stock suspension, uneven pipetting can cause a different amount of activity to be added to a dialysis tube. The measured count rates (in cpm) of the nanoparticles used for dialysis are displayed in table A.1 in Appendix A. According to table A.1, the count rate of the FeNPs added to tube C is lower than that of tube A or B by approximately a factor 4. Because the activity added to a tube is directly correlated to the amount of nanoparticles present inside the tube, there are fewer nanoparticles inside tube C, but the exact concentration is not known.
Similarly to the AgNPs, the ion release profile of the FeNPs used in this experiments appears to be linear. Tube A, B and C show an ion release rate of 0.0079%, 0.0091% and 0.0341% of the total nanoparticle weight per day, respectively. The ion release as indicated by the weight percentage by tube C therefore appears to be much greater than that of the other nanoparticles. However, if looked at in terms of the activity released, the ion release is much more similar between different tubes. After 28 days, the count rate of the sample taken from tube A was 430.64 cpm, that of tube B was 452.99 cpm and that of tube C 416.37 cpm. While the count rate of tube C was slightly lower, the calculated weight percentage is much higher due to tube C's lower initial activity.

The increased ion release rate observed in Tube C could be explained by its lower concentration compared to the other tubes. Nanoparticles in a suspension with a higher concentration are more likely to collide and therefore aggregate, while suspensions with lower concentration lead to less aggregation.
As a result of aggregation, the available surface area and reactivity of the nanoparticles decrease, and the ion release rate subsequently decreases too [85]. Therefore, the lower concentration of Tube C may actually lead to a higher ion release rate. However, it should be noted that this is only a hypothesis and it is not known whether the difference in concentration between tube C and the other two is significant enough for this to occur.
It is also important to note that the maximum ion release achieved after 28 days is 1.09%, which was observed in tube C. It is not known whether *S. aureus* bacteria can take up FeNPs with the same size as the nanoparticles used in this experiment.
If uptake of FeNPs is impossible, iron uptake in the presence of FeNPs can only occur through the iron uptake mechanisms discussed in section 2.3.1. Unless iron can be harvested from FeNPs by these mechanisms, they are limited to the iron ions released by the nanoparticle. These findings therefore put an upper limit on the iron uptake of bacteria if the previously mentioned assumptions hold true and if they are cultured in a medium containing FeNPs with a concentration of 500 µg/ml.
However, as was mentioned in section 4.1.5.1, the local environment plays an important role during nanoparticle ion release. In this experiment FeNPs were immersed in PBS, but a bacterial medium such as BHI would influence the ion release as well.

4.2 Method characterization

A number of different experiments were conducted to prepare for the irradiation of the nanoparticles, ion release experiments and bacterial growth experiments. Methods to separate the water and nanoparticles inside an IONP suspension were investigated and are discussed in section 4.2.1. Centrifuging and ultracentrifuging of different types of nanoparticles are discussed in sections 4.2.2 and 4.2.3 respectively.

4.2.1 IONP separation

A number of different experiments were conducted to determine the best method to remove IONPs from suspension, in order to prepare for the irradiation of said IONPs. The methods tested include freeze-drying, desiccation and centrifuging with an ultracentrifuge. An oven and ultrasonication were also used, as described in section 3.3. DLS was then performed to determine the size distribution before and after separation. The size distribution measurements obtained through DLS are displayed in figure 4.8. Freeze-drying, desiccation and ultracentrifugation are discussed separately in sections 4.2.2.1, 4.2.2.2 and 4.2.2.3 respectively.

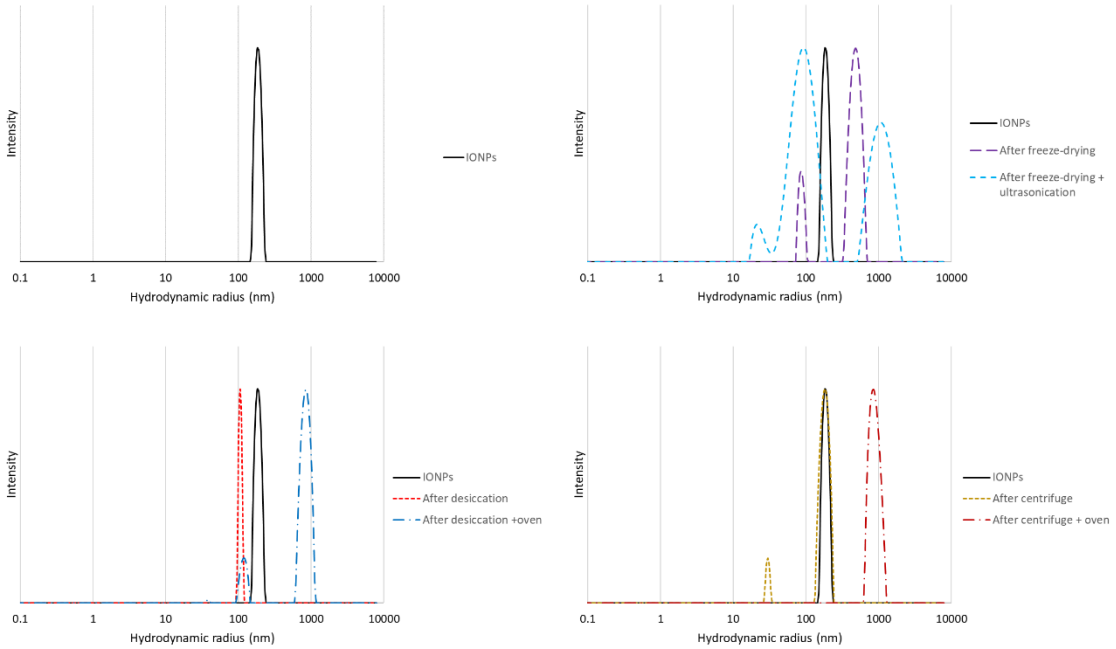

Figure 4.8: DLS size distributions of IONPs before separation (a), after freeze-drying (b), after desiccation (c) and after centrifuging (d).

4.2.2.1 Freeze-drying

During the sublimation step of the freeze-drying process, the frozen IONP suspension was observed to become liquid and the formation of bubbles took place as the water evaporated. The freeze-dryer achieved a pressure of 30 mTorr (4 Pa) and -45°C, conditions in which ice would sublimate. The exact mechanism that causes the bubbling is not known, but the presence of the IONPs or a surfactant likely causes this to happen.

As can be seen in figure 4.8b, the hydrodynamic radius of the IONPs increased from a peak of 181.7 nm to 481.8 nm after freeze-drying. However, a portion of the IONPs actually had a reduced hydrodynamic radius. After ultrasonication the hydrodynamic radius of the bulk of the nanoparticles decreases, as the peak at 90.6 nm indicates. However, the hydrodynamic radius of a portion of the IONPs actually increases to 1061.0 nm. The increase of the hydrodynamic radius is likely caused by aggregation due to the removal of the nanoparticle surfactant during ultrasonication. Freeze-drying was observed to lead to the aggregation of nanoparticles. The instability of nanoparticle suspensions during freeze-drying is a well known problem and it is suggested that the addition of an amorphous stabilizing matrix consisting of sugars such as trehalose and sucrose may stabilize nanoparticles during freeze-drying [86].

4.2.2.2 Desiccation

After the IONP sample was placed in the vacuum desiccator, some bubbling was observed, but not to the same extent as was observed during the freeze-drying mentioned in the previous section. After desiccation the mass of the sample was reduced by 0.996 g, corresponding to 0.998 ml of water (at room temperature). The mass of the IONPs in the sample, and therefore the mass of the remaining water inside the sample are not known.

While the mass of the remaining water inside the sample is not known exactly, approximately 1 ml of suspension was placed in the desiccator, and therefore it can be

assumed that more than 95% of the water of the sample was removed . As can be seen in figure 4.8c, the hydrodynamic radius of IONPs after resuspension was decreased compared to that of IONPs before desiccation. According to DLS the IONPs had a hydrodynamic radius close to 175 nm prior to desiccation, which decreased to 105 nm after resuspension. Some aggregation may have taken place in the regular IONP sample, while the resuspension of the IONPs in the other sample caused them to de-aggregate.
When the samples were placed in an oven after desiccation, no significant reduction of mass was observed. It was determined that only 0.2 mg of mass was removed by the oven, compared to the 0.998 grams removed after desiccation. As is displayed in figure 4.8c, the hydrodynamic radius of the IONPs increased greatly compared to the other samples. The hydrodynamic radius of the post-oven IONPs was measured to be 848.8 nm. This may be explained by the destruction of the surfactant present on the IONP surface by the heat inside the oven. The removal of the surfactant would cause aggregation, leading to the observed increase of the hydrodynamic radius. However, a small population of IONPs with a hydrodynamic radius similar to pre-oven IONPs remained. The observed increase in the particle size could also be ascribed to a small population of large IONP aggregates, as large particles are known to scatter more light. As these experiments were not performed in triplicate, it is more difficult to determine the amount of water removed from the sample with great accuracy. Because no significant IONP aggregation is observed after drying, and almost all of the water is removed, desiccation is a viable method to separate IONPs from water.

4.2.2.3 Ultracentrifugation

Ultracentrifugation was also performed to dry the IONPs. The mass of the sample was reduced by 1.22 g. As around 1.5 ml of the nanoparticle suspension was added, an estimated 80% of the water in the sample was removed. A small layer of water was indeed present inside the sample, which could not be removed without disturbing the IONP pellet. The water likely would have evaporated if the sample was air-dried for a longer period.
The size distribution of the IONPs was measured with DLS after resuspension. As can be seen in figure 4.8d, the DLS peak of IONPs after centrifuging is located at 183.4 nm, compared to the pre-centrifuge IONP peak at 175.1 nm. The use of an ultracentrifuge therefore resulted in IONPs that were very similar to IONPs before separation took place.
As with the desiccation experiment, a sample was also placed in an oven after ultracentrifugation. The oven removed a further 0.11 g of water. The use of an oven resulted in an increased hydrodynamic radius after resuspension, as a hydrodynamic radius of 848.8 nm was measured. This is the exact same result as the measured hydrodynamic radius after desiccation and oven. As no smaller population of IONPs is measured in the DLS measurements, the similar results are likely caused by aggregation as a result of the loss of surfactant in the oven, rather than a small number of aggregations scattering a lot of laser light. In future experiments, it would be worthwhile to sonicate the particles after drying, to determine if the hydrodynamic radius is reduced.

In summary, freeze-drying resulted in bubbling and caused the IONPs to stick to the tube walls, which made it difficult to ascertain the amount of water that was removed from the sample. Some aggregation was also observed, and the use of ultrasonication resulted in more aggregation.

Desiccation removed most of the water in the sample by far, and did not result in aggregation unless the samples were placed in the oven. Ultracentrifugation was unable to remove all of the water, primarily because the actual removal of the water relied on the use of a syringe, but ultracentrifuged IONPs were observed to have a similar hydrodynamic radius compared to IONPs before drying.
Based on these findings, it was determined that desiccation for 6 days proved to be the most effective method to remove the water from an IONP suspension. However, the presence of a surfactant may complicate the irradiation of IONPs, and it was therefore decided that irradiated FeNPs would be used for bacterial uptake experiments instead of radioactive IONPs.

4.2.2 Nanoparticle centrifuging

In order to prepare for the other experiments conducted in this thesis, experiments were performed to determine the optimal centrifuge settings to remove AgNPs, FeNPs, IONPs and ZnNPs from suspension. This was done by centrifuging the nanoparticles at different speeds for 10 minutes. The size distribution of the supernatant after centrifuging was measured using DLS. The average scattering intensity at full laser intensity was also recorded. The hydrodynamic radii and average scattering count rates are found in tables 4.3 and 4.4 respectively. The size distributions of particles after centrifuging are displayed in figure A.6 in Appendix A.

	AgNPs (nm)	FeNPs (nm)	IONPs (nm)	ZnNPs (nm)
0 x g	14.3, 72.4	144.6, 700.1	66.0, 422.7	151.6, 884.7
2000 x g	14.4, 166.9	191.1	19.7, 159.5	37.7, 383.7
4000 x g	12.4	109.5	15.7, 91.4, 704.5	114.8, 531.0
6000 x g	12.4, 350.9	884.4	24.8	75.6, 304.2
8000 x g	16.4, 291.5	114.7	17.2, 278.4	304.3
10000 x g	13.6, 231.1	95.3	18.9, 201.1	120.2, 927.1

Table 4.3: Peaks of the size distribution of nanoparticles in the supernatant after centrifuging at various speeds obtained through DLS. Hydrodynamic radii are indicated in nm.

Table 4.3 and figure A.6 show that the hydrodynamic radius of nanoparticles in the supernatant tends to decrease as the centrifuge speed increases. This is most clearly observed in silver, where a large peak at 72.4 nm shifts left to 13.6 nm as the centrifuge speed increases. The sedimentation rate of a particle can be explained by Stokes' law (eq. 6), where v refers to the sedimentation velocity of a sphere, d_c to the sphere's diameter, ΔP to the difference in density between the particle and medium, g to the gravitational force and η to the viscosity of the medium [87]. As eq. 6 shows, large particles will sediment quicker at lower speeds because the sedimentation rate depends quadratically on the particle diameter, while it linearly depends on the gravitational force (in this case the centrifuge speed).

Particles with large hydrodynamic radii, such as those formed by aggregation, experience a greater sedimentation speed than small particles and are therefore 'filtered out' by the centrifuge. This size-selection phenomenon can be used to isolate size-specific nanoparticle fractions to improve Magnetic Resonance Imaging performance [88].

$$v = \frac{{d_c}^2 \Delta P * g}{18\eta} \text{ eq. 6}$$

	AgNPs (kHz)	FeNPs (kHz)	IONPs (kHz)	ZnNPs (kHz)
2000 x g	506.0	851.4	161.5	25.1
4000 x g	297.4	451.3	167.1	146.7
6000 x g	221.7	231.8	106.5	206.7
8000 x g	267.2	37.55	206.8	255.1
10000 x g	358.0	24.2	142.5	71.84

Table 4.4: Scattering count rate obtained from DLS of different types of nanoparticles after centrifuging. These measurements were taken at maximum laser intensity. Count rates are indicated in kHz

Table 4.4 shows that the scattering count rate measured during DLS does not appear to be influenced by the centrifuge speed. Only for the FeNPs did the scattering intensity decrease as the centrifuge speed increased. It is important to note that measurements of nanoparticles before centrifuging could not be taken at full intensity, as doing so would damage the DLS equipment due to high scattering. However, these results show that particles are indeed present in the supernatant. It is likely that these are the nanoparticles used for this experiment, though another technique such as ICP-MS would have to be employed to verify this.
While the average scattering intensity is not an effective measure of the number of particles present in suspension, it does provide some information on the presence of nanoparticles. Methods such as turbidimetry or the use of a Coulter counter would have proven to be more effective methods to provide an estimate of the number of particles in suspension. However, due to the sensitivity of the ICP-MS and radiation counting devices used in other experiments in this thesis, it is important to remove all nanoparticles from suspension. Therefore, the ability to detect the presence of nanoparticles through the scattering count rate was decided to be enough.
It was concluded that the speeds of the centrifuge used for this experiment were not high enough to remove all nanoparticles from suspension.

4.2.3 Nanoparticle ultracentrifugation

As mentioned in section 4.2.2, the speeds of the Biofuge A centrifuge proved insufficient for the removal of nanoparticles from suspension. Therefore, separation experiments were conducted using an ultracentrifuge at 100.000 x g. After centrifuging DLS was performed at full laser intensity to measure the scattering count rate and nanoparticle size distribution. The peaks of the size distribution and the scattering count rate can be found in tables 4.5 and 4.6 respectively. The full size distribution graphs are displayed in figure A.7 in appendix A.

	Before centrifuge (nm)	After centrifuge (nm)
AgNP	47.7	91.4, 403.8
FeNP	83.3, 305.6	110.0, 773.2
IONP	43.5	145.4
ZnNP	2248.9	183.4

Table 4.5: Size distribution peaks obtained from DLS measurements before and after centrifugation of various types of metallic nanoparticles. The hydrodynamic radius is shown in units of nm.

Table 4.5 and figure A.7 show that in case of the AgNPs and IONPs, the measured hydrodynamic radius of the particles increases after they are centrifuged at 100,000 x g. In contrast, the hydrodynamic radius of the FeNPs and ZnNPs was observed to decrease after ultracentrifugation. The reduction of the hydrodynamic radius of the latter two may be explained by their low stability in suspension as discussed in more detail in the previous section. It is not known why the hydrodynamic radius of AgNP and IONP actually increases after centrifugation.

	After centrifuge (kHz)
AgNP	170.0
FeNP	113.0
IONP	65.2
ZnNP	73.1

Table 4.6: Average scattering count rate obtained from DLS measurements after centrifugation. The count rate is shown in units of kHz.

Table 4.6 shows that particles may still be present in the sample, as the count rate is higher than the background count rate of water of 5.18 kHz. The count rate of AgNP and FeNP is notably higher than that of the other two nanoparticles. AgNP particles are small, and therefore have a lower sedimentation rate as explained in the previous section. While more nanoparticles were removed from suspension than was shown in centrifugation experiments described in the previous section, these findings show that particles are still present inside the supernatant. As the DLS tubes were cleaned thoroughly with ethanol before sample preparation, the observed particles are likely nanoparticles. The goal of this experiment was to remove all nanoparticles from suspension, but it is likely that doing so through high-speed centrifugation is very difficult. Other experiments could be conducted to verify the presence of nanoparticles in the supernatant after ultracentrifugation, and to try to improve the removal of nanoparticles through techniques such as ultrafiltration.

4.3 *S. aureus* growth in the presence of nanoparticles

To determine the effect of AgNPs and FeNPs on the growth of bacteria, growth curve experiments were performed by measuring the optical density of samples at 600 nm (OD_{600}) using spectrophotometry.

A growth curve was then constructed, and the logistic growth equation (eq.1) mentioned in section 2.3.2 was fitted to the curve by way of the damped least-squares method and the three unknown growth parameters were thus calculated. The findings concerning bacterial growth in the presence of AgNPs and FeNPs are described in section 4.3.1 and section 4.3.2 respectively.

4.3.1 AgNP growth curve

The influence of various concentrations of AgNPs on bacterial growth was investigated through growth curve experiments. Figure 4.9 displays the mean of the OD_{600} of samples that were taken over time, as well as the curve obtained through least-squares regression. Table 4.8 summarises the estimated growth parameters obtained from the regression curve.

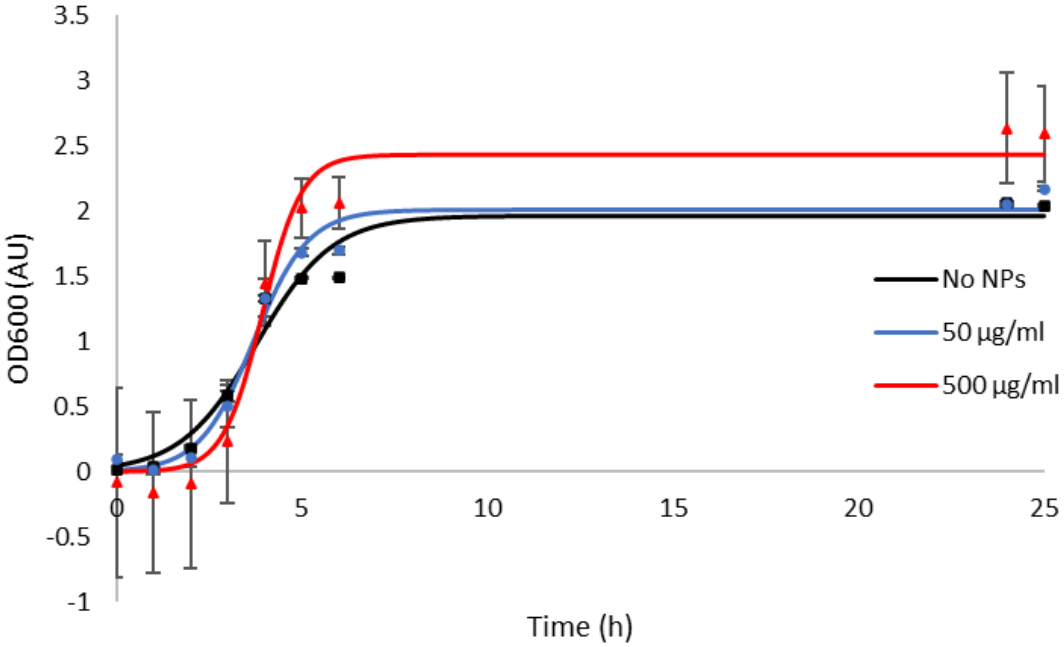

Figure 4.9: Growth behaviour of *S. aureus* in the presence of various concentrations of AgNPs. Different markers represent the mean (n = 3) of samples taken, while the error bars represent one standard deviation from the mean. The lines represent the curves obtained through fitting.

Nanoparticle concentration	$OD_{600,max}$ (AU)	μ_{max} (h^{-1})	t_i (h)
0 µg/ml	1.96 ± 0.11	0.98 ± 0.21	3.78 ± 0.27
50 µg/ml	2.01 ± 0.09	1.37 ± 0.26	3.7 ± 0.17
500 µg/ml	2.43 ± 0.13	1.89 ± 0.57	3.94 ± 0.18

Table 4.7: Estimated growth parameters of *S. aureus* when cultured in the presence of various concentrations of AgNPs.

As can be seen in figure 4.9, the initial OD_{600} differed somewhat between the different samples. The mean of the initial OD_{600} of the 500 µg/ml sample was determined to be -0.08 ± 0.73 AU. If the OD_{600} of a sample is negative, that indicates that the optical density of the sample was lower than the reference. However, the concentration of nanoparticles inside the sample also influences the measured OD_{600}. The OD_{600} at t = 0 h is representative of the initial number of bacteria in a culture flask. However, it is unlikely that the high standard deviation is caused by large variations in the number of bacteria, as the bacterial medium was inoculated with 250 µl of preculture in every culture flask.

It is more likely that the high standard deviation that is observed at all OD_{600} measurements of the 500 µg/ml group is caused by variations in the concentration of silver nanoparticles.
The maximum growth rate (μ_{max}) and maximum cell density ($OD_{600,max}$) appear to increase as the nanoparticle concentration increases, as displayed in table 4.7. These findings seemingly suggest that AgNPs aid in the growth of *S. aureus*. However, this is in stark contrast to previous studies, which show that AgNPs exhibit antimicrobial activity against *S. aureus*, as described in section 2.2.1 [22, 55].
It is important to note that the measurement of the OD_{600} relies on the scattering of light by particles inside the sample, the size and shape of cells inside sample, as well as the presence of other particles and dead cells influence the measured optical density []. It is known that larger particles scatter more light than small particles [76]. If aggregates of AgNPs form, or AgNPs bind to the surface of *S. aureus* (though this is less likely due to the zeta potential of both particle and bacterium), the greater particle size may hypothetically lead to more scattering, resulting in a higher OD_{600}. Increased scattering as a result of nanoparticle aggregation on the cell surface was observed in a previous study involving gold nanoparticles and *Escherichia coli* [89].
As mentioned previously, the ion release of silver nanoparticles at 500 µg/ml is relatively slow, as the concentration of silver ions is measured to be 1.28 µg/ml after 24 hours, a similar timeframe as the growth curve experiments. Ion release is one of the main mechanisms of antibacterial action by AgNPs. The slow ion release of the AgNPs may contribute to the observed reduction of their efficacy against bacteria.
Finally, a recent study has shown that AgNPs do not always exhibit antibacterial activity against *S. aureus* [90]. In this study the AgNPs were of a similar size as the ones used for this experiment, and a similar zeta potential at -40 mV. It is suggested that the cell-wall structure of bacteria may lead to a different sensitivity to AgNPs. As *S. aureus* is a gram-positive bacterium with cell wall that possesses a zeta potential of -10 mV [90], the negative charge of the bacterial cell wall may hypothetically repel the negatively charged AgNPs, partially preventing cellular uptake, another antimicrobial mechanism.
In summary, while the addition of AgNPs to the culture medium resulted in an increase of the $OD_{600,max}$ and μ_{max}, it is unlikely that these bacteria experience increased growth due to the supplementation of the AgNPs. The observed findings can alternatively be explained by a combination of scattering resulting in a higher measured OD_{600}, and a number of mechanisms which reduce the antimicrobial efficacy of the AgNPs. To verify these results, experiments with other techniques to measure bacterial growth could be conducted.

4.3.2 FeNP growth curve

Growth curve experiments were conducted to determine the influence of FeNPs on the growth of *S. aureus*. Figure 4.10 displays the mean of the OD_{600} of samples that were taken to construct a growth curve, as well as the curve obtained through weighted least-squares regression. Table 4.8 shows the growth parameters obtained through curve fitting.

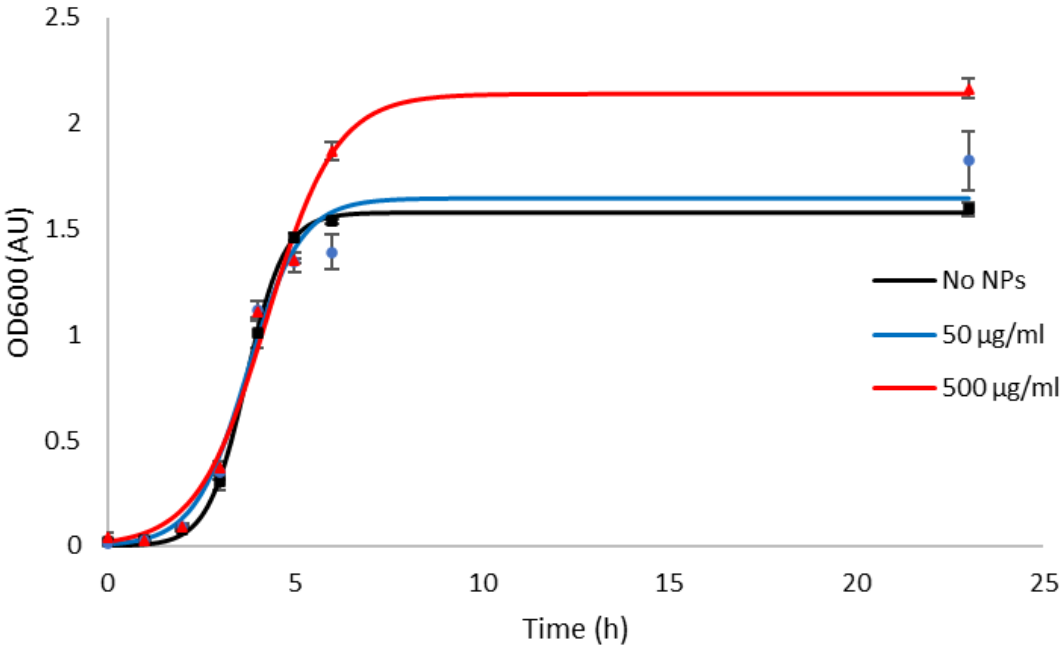

Figure 4.10: Growth behaviour of *S. aureus* when crown in the presence of FeNPs. Different colours represent the different concentrations of FeNPs, while the lines represent the growth curves obtained through regression. The error bars represent one standard deviation from the mean (n = 3)

Nanoparticle concentration	$OD_{600,max}$ (AU)	μ_{max} (h^{-1})	t_i (h)
0 µg/ml	1.58 ± 0.01	1.94 ± 0.08	3.71 ± 0.03
50 µg/ml	1.64 ± 0.11	1.41 ± 0.36	3.74 ± 0.23
500 µg/ml	2.14 ± 0.11	1.08 ± 0.02	4.25 ± 0.18

Table 4.8: Estimated growth parameters of *S. aureus* growth behaviour when grown in the presence of FeNPs.

Similarly to the AgNP growth curve experiment, the $OD_{600,max}$ was observed to increase when the FeNP concentration increases. However, the maximum growth rate μ_{max} of the bacteria actually decreases as the nanoparticle concentration increases. The estimated maximum growth rate of bacteria grown with 500 µg/ml of FeNPs is 44% lower than that of the control group without nanoparticles. This may indicate some antibacterial activity, but the maximum OD_{600} of the 500 µg/ml group actually increases by 85% compared to the 0 µg/ml group. If FeNPs do exhibit antibacterial activity the maximum OD_{600} would decrease as the concentration increases. *S. aureus* growth in BHI medium may be limited by iron, and FeNPs could provide a source of iron for the bacteria to use. The slow ion release rate of FeNPs would limit bacterial uptake and therefore limit growth. This may explain why the maximum growth rate is lower, as it takes more time for the bacteria to reach the maximum optimal density.
As mentioned in the previous section, the OD_{600} is a measure of the amount of scattering in a sample, rather than absorption. If nanoparticles inside the sample aggregate, the increased particle size may lead to greater scattering. This could serve as an alternative explanation for the observed increase of the OD_{600}.

If this is indeed the case, observed increases of the maximum bacterial density may simply be ascribed to the nanoparticles, and the maximum growth rate would because of the way it is calculated, rather than a decrease in the bacterial growth rate. It can therefore not be concluded whether FeNPs affects the growth behaviour of *S. aureus*. Experiments with other techniques to measure the bacterial growth, such as the counting of CFUs, would have to be conducted to elucidate these findings.

4.4 *S. aureus* iron uptake

This section describes the experiments conducted to determine the ^{59}Fe uptake of *S. aureus*. In section 4.4.1, factors used to correct for the geometric effects on the measured activity due to differences in volume are determined. In sections 4.4.2 and 4.4.3, the findings of the iron uptake experiments are discussed.

4.4.1 Determining volume correction factors

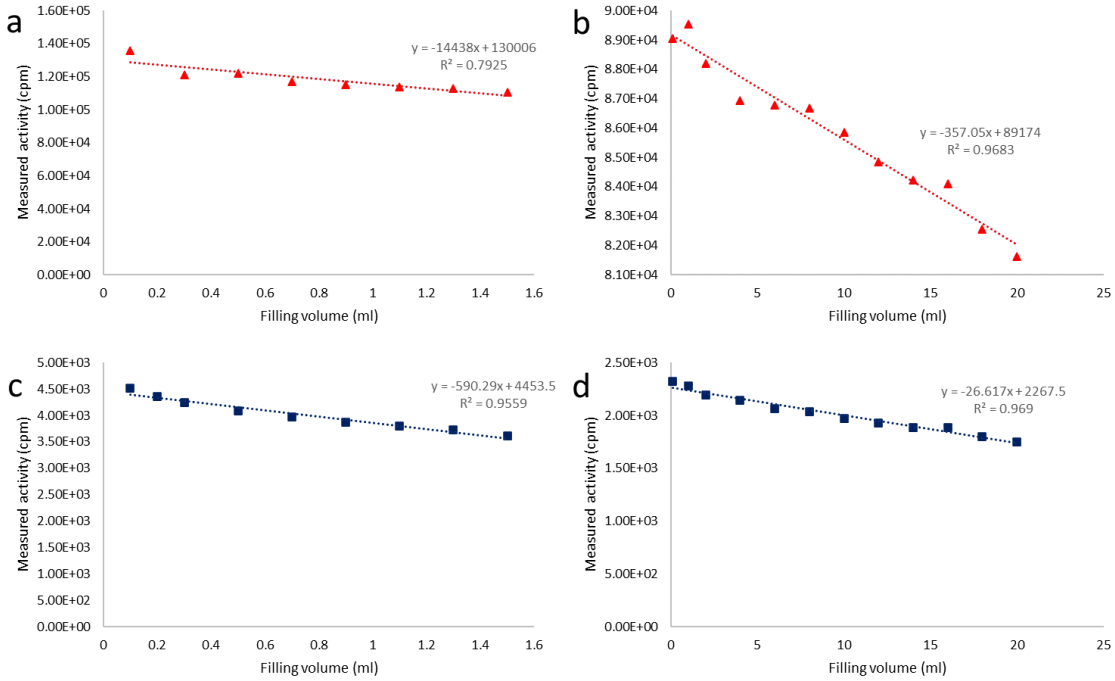

Figure 4.11: The effect of the filling volume of a sample consisting of ^{rad}FeNPs in an Eppendorf tube (a), ^{rad}FeNPs in a 20 ml counting vial (b), radioactive iron ions in an Eppendorf tube (c) and radioactive iron ions in a 20 ml counting vial (d) on the measured activity by the Wallac gamma counter.

Due to the sensitivity of the Wallac Gamma Counter employed in this thesis to geometric effects that arise from the sample volume, experiments were conducted to determine the factors necessary to correct for these effects. The sample volume of a sample consisting of radioactive FeNps or ions was changed, after which the count rate was measured.

The count rates after measuring are displayed in figure 4.11. A trend line with the general formula y = ax + b was fitted to the graph using Microsoft Excel.

The volume correction factors F_{cor} were calculated by dividing the slope **a** of the obtained trendline by the estimated count rate at a filling volume of 0 **b**, according to the formula
$F_{cor} = -a/b$. For the ^{rad}FeNPs in an Eppendorf tube and 20 ml glass counting vial, the obtained correction factors were calculated to be $F_{cor} = 0.11$ and $F_{cor} = 0.004$ respectively. In case of the radioactive iron ion sample, the calculated correction factors were $F_{cor} = 0.13$ for the 1.5 ml Eppendorf tube, and F_{cor} 0.012 for the glass counting vial. These correction factors were applied in both the ion release and iron uptake experiments.

4.4.2 Nanoparticle iron uptake

In order to determine the uptake of iron released from iron nanoparticles by *S. aureus*, experiments were conducted whereby growth medium inoculated with *S. aureus* was supplemented with ^{rad}FeNPs. The bacteria were then allowed to grow overnight, after which the nanoparticles were removed through a combination of sedimentation and centrifugation and the uptake was measured by way of a Wallac Gamma Counter. To determine the correct count rates, the correction factors obtained in the previous section were employed, and half-life correction was performed. The iron uptake of bacteria is defined as the percentage of the supplemented activity that remained after. OD_{600} measurements were also taken after growth.
The uptake of nanoparticle-released iron by *S. aureus* was measured to be very limited. The mean uptake of iron was calculated to be only 4.2 ± 2.4%. However not all ^{rad}FeNPs are removed by the nanoparticle removal protocol. An mean of 0.5% of the ^{rad}FeNPs is estimated to remain in the bacterial culture as shown in Appendix B.2. Therefore, the mean uptake of iron is closer to 3.7%. The low uptake rate is likely caused by the slow release of iron ions by ^{rad}FeNPs, as shown in section 4.1.5.2. Remarkably, the iron uptake found in this experiment is greater than the maximum wt% of released iron found in section 4.1.5.2, as the uptake was measured to be 3.7% while the maximum iron ion release was found to be approximately 1% in one specific case after 28 days. The discrepancy between the iron ion release and iron uptake may have a number of different causes. Firstly, a greater number of ^{rad}FeNPs may stay behind in the sample than the 0.5% originally measured with the centrifuge experiment, possibly through nanoparticle-to-cell contact. Secondly *S. aureus* may hypothetically take up parts of or the whole nanoparticle, as this was already observed to occur with AgNPs [56]. Due to the size of the nanoparticles used in this experiment and the bacterial cell wall this is unlikely, but is a possibility that should be investigated further. The increased uptake may also be explained by *S. aureus* iron uptake mechanisms taking iron from the ^{rad}FeNPs directly, rather than being limited to released ions as their only source of radioactive iron. Siderophores are known to increase the solubility of iron oxide which may play a role in iron acquisition by marine and terrestrial organisms [91].
The OD_{600} after overnight growth was also measured and is displayed in table 4.9. Table 4.9 shows that the OD_{600} after overnight growth increased most if the medium was supplemented with non-radioactive FeNPs. The OD_{600} of bacteria grown in the presence of ^{rad}FeNPs did not increase significantly compared to the control group. The differences between the bacteria supplemented with ordinary FeNPs and ^{rad}FeNPs may be ascribed to a difference in the concentration of nanoparticles. The non-radioactive FeNP suspension was made by suspending FeNPs in water, while the ^{rad}FeNP suspension was created by combining a non-radioactive FeNP suspension with ^{rad}FeNPs.

In theory, these should have the same concentration of 25 mg/ml, but practice has shown that FeNPs are unstable in suspension and differences in concentration between samples occur easily.

	OD_{600} (AU)
Control	1.84 ± 0.12
FeNPs	2.10 ± 0.02
Radioactive FeNPs	1.89 ± 0.16

Table 4.9: Mean OD_{600} of bacterial cultures after overnight growth supplemented with FeNPs or ^{rad}FeNPs

These findings establish that *S. aureus* takes up 3.7 ± 2.4% of the iron from nanoparticles, but the question remains whether this uptake percentage is unique to nanoparticle iron, or is also observed when iron is supplemented in a different form. Therefore, experiments must be performed to determine the uptake percentage of iron supplied in the form of iron ions.

4.4.3 Iron ion uptake

To determine whether the low iron uptake discussed in the previous section was because the iron was supplied in the form of iron nanoparticles, experiments were undertaken where bacteria were supplied with radioactive iron ions. As in the previous experiment, the bacteria were allowed to grow overnight (24 hours) and the remaining radioactive iron was removed through centrifuging. The remaining activity was measured and corrected through half-life and volume correction. The OD_{600} after overnight growth was also measured.

The iron ion uptake of *S. aureus* was measured to be significantly higher than ^{rad}FeNP-sourced iron uptake. The mean uptake of iron ions was calculated to be 53.3% ± 12.4%. The obtained percentage is an order of magnitude greater than the uptake percentage of nanoparticle-source iron, confirming that the form of iron supplemented to bacteria affects its uptake. The low uptake of nanoparticle iron is therefore most likely caused by the low release rate of iron ions by the ^{rad}FeNPs.

In table 4.10 it is shown that the OD_{600} of bacteria supplemented with radioactive ions is similar to that of the control group after overnight growth. In contrast to the findings discussed in the previous section, the mean OD_{600} of bacteria supplemented with Fe ions was lower compared to the other two groups, but still within one standard deviation of the control group. These results therefore show that *S. aureus* seems to take up and utilize both regular iron and ^{59}Fe. To investigate this further, experiments with techniques such as ICP-MS could be conducted.

	OD_{600} (AU)
Control	1.76 ± 0.61
Fe ions	1.69 ± 0.09
Radioactive ions	1.80 ± 0.12

Table 4.10: OD_{600} of bacteria after overnight growth when supplemented with radioactive iron

5. Conclusions and recommendations

5.1 Conclusions

The aim of this thesis was to investigate the uptake of iron released from iron nanoparticles by *S. aureus* bacteria. To answer this question, several different kinds of nanoparticles were characterized, bacterial growth in the presence of nanoparticles was investigated, and the uptake of nanoparticle-sourced and free ^{59}Fe was quantified. Firstly, silver, iron, iron oxide and zinc nanoparticles were characterized to determine several different properties. Through the use of DLS, it was discovered that both FeNPs and ZnNPs form unstable suspensions and sediment easily, while AgNps and IONPs form stable suspensions and aggregate little. XRD was then performed to investigate the composition of the nanoparticle. Fe_3O_4 and ZnO peaks were found in the XRD patterns of FeNPs and ZnNPs respectively, indicating a partial oxidation of the aforementioned nanoparticles. No significant oxidation of AgNPs was found through XRD. AgNPs and FeNPs were also examined with TEM, where it was observed that the AgNPs and FeNps had an average size of approximately 14 and 75 nm respectively. The zeta potential of all nanoparticles in MQ was measured through the use of a Zetasizer. It was determined that the AgNPs had the lowest zeta potential, which is consistent with the observation that they formed the most stable suspensions. The ion release of AgNPs and FeNPs was measured through the use of ICP-MS and gamma counting of ^{59}Fe, respectively. The cumulative ion release was found to be 1% for AgNPs after 4 days and a maximum of 1% for FeNPs after 28 days. A number of methods were investigated to remove IONPs from suspension, of which it was found that desiccation for 6 days was the most effective technique, as nearly all of the water was removed while no aggregation was observed. Centrifugation and ultracentrifugation were also attempted to remove several different types of nanoparticles from suspension, but no satisfactory protocol was found. The growth behaviour of *S. aureus* when grown in a medium supplemented with various concentrations of AgNPs and FeNPs was investigated. It was found that the maximum growth rate of *S. aureus* increased in the presence of AgNPs while it decreased in the presence of FeNPs. The $OD_{600,max}$ increased when *S. aureus* was supplemented with either type of nanoparticle. It is not known whether the observed increases of the OD_{600} are the result of bacterial growth or a fault in the growth measuring method. Finally, the uptake of ^{59}Fe by *S. aureus* was measured by gamma counting. It was discovered that only 3.7 ± 2.4% of iron released from nanoparticles was taken up by *S. aureus*. If the iron was supplemented in an ionic form, the iron uptake was measured to be 53.3 ± 12.4%.It was therefore concluded that nanoparticle-released iron uptake is primarily limited by the low release rate of ions from FeNPs. It is important to note that the FeNP iron uptake percentage was found to be greater than the observed ion release after a period of 24 hours. It is not known whether this is the result of bacterial-FeNP contact which allows FeNPs to evade the centrifugation step, because *S. aureus* can take up either parts of or the whole nanoparticle, or direct iron scavenging from the nanoparticle by *S. aureus*' iron uptake mechanisms.

The main research question was whether *S. aureus* can take up and utilize iron supplied in the form of nanoparticles. While it is clear that the uptake of iron by *S. aureus* greatly depends on the form in which that iron is supplied, it has not yet been determined whether nanoparticle iron is actually taken up by the bacteria. It is also not clear whether the supplemented iron can contribute to bacterial growth.

5.2 Recommendations

While this thesis did establish that the form in which iron is supplemented influences its uptake by *S. aureus*, a number of questions still remain. Firstly, properties such as the hydrodynamic radius, zeta potential and ion release should be characterized if AgNPs and FeNPs are suspended in Brain Heart Infusion medium. The results obtained from such experiments could elucidate some of this thesis' findings. However, contamination of the experiments by bacteria may lead to rapid bacterial growth which would affect the obtained results. This is likely to happen in the case of long-term ion release experiments, and dialysis may have to be performed in a sterilized environment to prevent this.

Secondly, while the attempts to remove water from the IONP suspension were successful, it was decided that FeNPs were to be used in ion release and bacterial uptake experiments, as the IONP surfactant layer complicated their irradiation. Removing the IONP surfactant layer causes aggregation. Rather than irradiating dried IONPs, IONPs may instead be synthesized from ^{59}Fe ions. A number of protocols to synthesize IONPs exist, such as the co-precipitation of Fe^{2+} and Fe^{3+} through the addition of NaOH [92]. Synthesized IONPs may then be used for ion release and bacterial uptake experiments.

Thirdly, the FeNPs used in this research project proved to form highly unstable suspensions. The addition of a surfactant may increase their stability and therefore make future experiments more consistent if repeated.

Fourthly, it is not yet clear whether the observed increase of the maximum OD_{600} during the growth curve experiments is caused by bacterial growth or some other cause such as nanoparticle aggregation. Rather than measuring the OD_{600}, other bacterial growth monitoring techniques such as the measurement of the dry weight (though this is complicated by the nanoparticles) or plate counting could be employed to provide a more accurate assessment of the growth of bacteria in the presence of nanoparticles.

Fifthly, while the experiments in this thesis did measure the bacterial uptake (defined as the percentage of remaining activity after the nanoparticle removal protocol), the percentage of iron that is internalized by the bacteria is not yet known. Even after washing, iron in the form of ions or membrane may be attached to the bacterial cell wall and can therefore not be used for growth. To study the internalization of iron, bacteria may be lysed after growth. If the membrane debris is then removed through filtration or centrifugation, the activity inside the remaining parts of the cell may then be measured to determine the degree of internalization of iron [31].

If the internalization rate of ^{59}Fe has been investigated, techniques such as the MIRAGE metalloproteomics approach can then be employed to determine the subcellular distribution of supplemented iron and its effect on the metabolism and growth of *S. aureus* [93].

Finally, the reason for the investigation of the nanoparticle-released iron uptake by bacteria was to develop an antimicrobial coating based on superparamagnetic iron oxide nanoparticles. Therefore, the attachment of radioactive iron or iron oxide nanoparticles to implants can also be investigated, so that a new antimicrobial coating may be developed to prevent the infection of medical implants by *S. aureus*.

Literature

1. Shichman, I., Roof, M., Askew, N., Nherera, L., Rozell, J. C., Seyler, T. M., & Schwarzkopf, R. (2023). Projections and Epidemiology of Primary Hip and Knee Arthroplasty in Medicare Patients to 2040-2060. *JBJS Open Access*, *8*(1).
2. Kelmer, G., Stone, A. H., Turcotte, J., & King, P. J. (2021). Reasons for revision: primary total hip arthroplasty mechanisms of failure. *JAAOS-Journal of the American Academy of Orthopaedic Surgeons*, *29*(2), 78-87.
3. Delaunay, C., Hamadouche, M., Girard, J., & Duhamel, A. (2013). What are the causes for failures of primary hip arthroplasties in France?. *Clinical Orthopaedics and Related Research*®, *471*(12), 3863-3869.
4. Kenney, C., Dick, S., Lea, J., Liu, J., & Ebraheim, N. A. (2019). A systematic review of the causes of failure of Revision Total Hip Arthroplasty. *Journal of orthopaedics*, *16*(5), 393-395.
5. Bozic, K. J., Kurtz, S. M., Lau, E., Ong, K., Chiu, V., Vail, T. P., ... & Berry, D. J. (2010). The epidemiology of revision total knee arthroplasty in the United States. *Clinical Orthopaedics and Related Research*®, *468*, 45-51.
6. Ahmed, S. S., & Haddad, F. S. (2019). Prosthetic joint infection. *Bone & Joint Research*, *8*(11), 570-572.
7. Tande, A. J., & Patel, R. (2014). Prosthetic joint infection. *Clinical microbiology reviews*, *27*(2), 302-345.
8. Camps-Font, O., Martín-Fatás, P., Clé-Ovejero, A., Figueiredo, R., Gay-Escoda, C., & Valmaseda-Castellón, E. (2018). Postoperative infections after dental implant placement: Variables associated with increased risk of failure. *Journal of Periodontology*, *89*(10), 1165-1173.
9. Fischbacher, A., & Borens, O. (2019). Prosthetic-joint infections: mortality over the last 10 years. *Journal of bone and joint infection*, *4*(4), 198-202.
10. Premkumar, A., Kolin, D. A., Farley, K. X., Wilson, J. M., McLawhorn, A. S., Cross, M. B., & Sculco, P. K. (2021). Projected economic burden of periprosthetic joint infection of the hip and knee in the United States. *The Journal of arthroplasty*, *36*(5), 1484-1489.
11. Campoccia, D., Montanaro, L., & Arciola, C. R. (2006). The significance of infection related to orthopedic devices and issues of antibiotic resistance. *Biomaterials*, *27*(11), 2331-2339.
12. Donlan, R. M. (2002). Biofilms: microbial life on surfaces. *Emerging infectious diseases*, *8*(9), 881.
13. Ricciardi, B. F., Muthukrishnan, G., Masters, E., Ninomiya, M., Lee, C. C., & Schwarz, E. M. (2018). Staphylococcus aureus evasion of host immunity in the setting of prosthetic joint infection: biofilm and beyond. *Current reviews in musculoskeletal medicine*, *11*, 389-400.
14. Stewart, P. S. (2002). Mechanisms of antibiotic resistance in bacterial biofilms. *International journal of medical microbiology*, *292*(2), 107-113.
15. O'Neill, J. (2016). Tackling drug-resistant infections globally: final report and recommendations.
16. Peel, T. N., Cheng, A. C., Buising, K. L., & Choong, P. F. (2012). Microbiological aetiology, epidemiology, and clinical profile of prosthetic joint infections: are current antibiotic prophylaxis guidelines effective?. *Antimicrobial agents and chemotherapy*, *56*(5), 2386-2391.
17. Iannotti, F., Prati, P., Fidanza, A., Iorio, R., Ferretti, A., Pèrez Prieto, D., ... & Indelli, P. F. (2020). Prevention of periprosthetic joint infection (PJI): a clinical practice protocol in high-risk patients. *Tropical medicine and infectious disease*, *5*(4), 186.
18. Cloutier, M., Mantovani, D., & Rosei, F. (2015). Antibacterial coatings: challenges, perspectives, and opportunities. *Trends in biotechnology*, *33*(11), 637-652.
19. Hosnedlova, B., Kabanov, D., Kepinska, M., B Narayanan, V. H., Parikesit, A. A., Fernandez, C., ... & Kizek, R. (2022). Effect of Biosynthesized Silver Nanoparticles on Bacterial Biofilm Changes in S. aureus and E. coli. *Nanomaterials*, *12*(13), 2183.

20. Erci, F., Cakir-Koc, R., Yontem, M., & Torlak, E. (2020). Synthesis of biologically active copper oxide nanoparticles as promising novel antibacterial-antibiofilm agents. *Preparative Biochemistry & Biotechnology*, *50*(6), 538-548.
21. Bianchini Fulindi, R., Domingues Rodrigues, J., Lemos Barbosa, T. W., Goncalves Garcia, A. D., de Almeida La Porta, F., Pratavieira, S., ... & Martinez, L. R. (2023). Zinc-Based Nanoparticles Reduce Bacterial Biofilm Formation. *Microbiology Spectrum*, *11*(2), e04831-22.
22. van Hengel, I. A., Tierolf, M. W., Fratila-Apachitei, L. E., Apachitei, I., & Zadpoor, A. A. (2021). Antibacterial titanium implants biofunctionalized by plasma electrolytic oxidation with silver, zinc, and copper: A systematic review. *International journal of molecular sciences*, *22*(7), 3800.
23. Sikdar, S., Menezes, P. V., Maccione, R., Jacob, T., & Menezes, P. L. (2021). Plasma electrolytic oxidation (PEO) process—processing, properties, and applications. *Nanomaterials*, *11*(6), 1375.
24. Thukkaram, M., Sitaram, S., & Subbiahdoss, G. (2014). Antibacterial efficacy of iron-oxide nanoparticles against biofilms on different biomaterial surfaces. *International Journal of biomaterials*, *2014*.
25. Tong, S., Quinto, C. A., Zhang, L., Mohindra, P., & Bao, G. (2017). Size-dependent heating of magnetic iron oxide nanoparticles. *ACS nano*, *11*(7), 6808-6816.
26. Alumutairi, L., Yu, B., Filka, M., Nayfach, J., & Kim, M. H. (2020). Mild magnetic nanoparticle hyperthermia enhances the susceptibility of Staphylococcus aureus biofilm to antibiotics. *International journal of hyperthermia*, *37*(1), 66-75.
27. Wu, L., Wen, W., Wang, X., Huang, D., Cao, J., Qi, X., & Shen, S. (2022). Ultrasmall iron oxide nanoparticles cause significant toxicity by specifically inducing acute oxidative stress to multiple organs. *Particle and Fibre Toxicology*, *19*(1), 1-14.
28. Hammer, N. D., & Skaar, E. P. (2011). Molecular mechanisms of Staphylococcus aureus iron acquisition. *Annual review of microbiology*, *65*, 129-147.
29. Dauros-Singorenko, P., Wiles, S., & Swift, S. (2020). Staphylococcus aureus biofilms and their response to a relevant in vivo iron source. *Frontiers in Microbiology*, *11*, 509525.
30. COPP, D. H., & GREENBERG, D. M. (1946). A tracer study of iron metabolism with radioactive iron; methods: absorption and excretion of iron. *The Journal of biological chemistry*, *164*, 377–387.
31. van Dijk, M.C. Iron & Infection, ^{55}Fe-MIRAGE to determine the impact of a sepsis-like pH 7.0 on the growth behaviour and iron metalloproteome of *Staphylococcus aureus*. Master's thesis. Delft University of Technology, 2021.
32. Ribeiro, M., Monteiro, F. J., & Ferraz, M. P. (2012). Infection of orthopedic implants with emphasis on bacterial adhesion process and techniques used in studying bacterial-material interactions. *Biomatter*, *2*(4), 176-194.
33. Wertheim, H. F., Melles, D. C., Vos, M. C., van Leeuwen, W., van Belkum, A., Verbrugh, H. A., & Nouwen, J. L. (2005). The role of nasal carriage in Staphylococcus aureus infections. *The Lancet infectious diseases*, *5*(12), 751-762.
34. Kalmeijer, M. D., van Nieuwland-Bollen, E., Bogaers-Hofman, D., de Baere, G. A., & Kluytmans, J. A. (2000). Nasal carriage of Staphylococcus aureus: is a major risk factor for surgical-site infections in orthopedic surgery. *Infection Control & Hospital Epidemiology*, *21*(5), 319-323.
35. Chen, A. F., Wessel, C. B., & Rao, N. (2013). Staphylococcus aureus screening and decolonization in orthopaedic surgery and reduction of surgical site infections. *Clinical Orthopaedics and Related Research®*, *471*, 2383-2399.
36. Peng, Q., Tang, X., Dong, W., Sun, N., & Yuan, W. (2022). A review of biofilm formation of Staphylococcus aureus and its regulation mechanism. *Antibiotics*, *12*(1), 12.
37. Ren, Y., Wang, C., Chen, Z., Allan, E., van der Mei, H. C., & Busscher, H. J. (2018). Emergent heterogeneous microenvironments in biofilms: substratum surface heterogeneity and bacterial adhesion force-sensing. *FEMS microbiology reviews*, *42*(3), 259-272.

38. Kreve, S., & Dos Reis, A. C. (2021). Bacterial adhesion to biomaterials: What regulates this attachment? A review. *Japanese Dental Science Review*, *57*, 85-96.
39. Katsikogianni, M., & Missirlis, Y. F. (2004). Concise review of mechanisms of bacterial adhesion to biomaterials and of techniques used in estimating bacteria-material interactions. *Eur Cell Mater*, *8*(3), 37-57.
40. Franz, S., Rammelt, S., Scharnweber, D., & Simon, J. C. (2011). Immune responses to implants–a review of the implications for the design of immunomodulatory biomaterials. *Biomaterials*, *32*(28), 6692-6709.
41. Hudson, M. C., Ramp, W. K., & Frankenburg, K. P. (1999). Staphylococcus aureus adhesion to bone matrix and bone-associated biomaterials. *FEMS microbiology letters*, *173*(2), 279-284.
42. Gristina, A. G. (1987). Biomaterial-centered infection: microbial adhesion versus tissue integration. *Science*, *237*(4822), 1588-1595.
43. López, D., Vlamakis, H., & Kolter, R. (2010). Biofilms. *Cold Spring Harbor perspectives in biology*, *2*(7), a000398.
44. Otto, M. (2013). Staphylococcal infections: mechanisms of biofilm maturation and detachment as critical determinants of pathogenicity. *Annual review of medicine*, *64*, 175-188.
45. Arciola, C. R., Campoccia, D., Ravaioli, S., & Montanaro, L. (2015). Polysaccharide intercellular adhesin in biofilm: structural and regulatory aspects. *Frontiers in cellular and infection microbiology*, *5*, 7.
46. Silva, V., Capelo, J. L., Igrejas, G., & Poeta, P. (2022). Molecular mechanisms of antimicrobial resistance in Staphylococcus aureus biofilms. *Emerging Modalities in Mitigation of Antimicrobial Resistance*, 291-314.
47. Kogan, G., Sadovskaya, I., Chaignon, P., Chokr, A., & Jabbouri, S. (2006). Biofilms of clinical strains of Staphylococcus that do not contain polysaccharide intercellular adhesin. *FEMS microbiology letters*, *255*(1), 11-16.
48. Mann, E. E., Rice, K. C., Boles, B. R., Endres, J. L., Ranjit, D., Chandramohan, L., ... & Bayles, K. W. (2009). Modulation of eDNA release and degradation affects Staphylococcus aureus biofilm maturation. *PloS one*, *4*(6), e5822.
49. Miller, M. B., & Bassler, B. L. (2001). Quorum sensing in bacteria. *Annual Reviews in Microbiology*, *55*(1), 165-199.
50. Schilcher, K., & Horswill, A. R. (2020). Staphylococcal biofilm development: structure, regulation, and treatment strategies. *Microbiology and Molecular Biology Reviews*, *84*(3), 10-1128.
51. Costerton, J. W., Stewart, P. S., & Greenberg, E. P. (1999). Bacterial biofilms: a common cause of persistent infections. *science*, *284*(5418), 1318-1322.
52. Prinzi, A., & Rohde, R. (2023). The role of bacterial biofilms in antimicrobial resistance. *ASM. org-American Society for Microbiology*.
53. Lewis, K. (2008). Multidrug tolerance of biofilms and persister cells. *Bacterial biofilms*, 107-131.
54. Sahoo, J., Sarkhel, S., Mukherjee, N., & Jaiswal, A. (2022). Nanomaterial-Based Antimicrobial Coating for Biomedical Implants: New Age Solution for Biofilm-Associated Infections. *ACS omega*, *7*(50), 45962-45980.
55. Wang, H., Wang, M., Xu, X., Gao, P., Xu, Z., Zhang, Q., ... & Sun, H. (2021). Multi-target mode of action of silver against Staphylococcus aureus endows it with capability to combat antibiotic resistance. *Nature communications*, *12*(1), 3331.
56. Yin, I. X., Zhang, J., Zhao, I. S., Mei, M. L., Li, Q., & Chu, C. H. (2020). The antibacterial mechanism of silver nanoparticles and its application in dentistry. *International journal of nanomedicine*, 2555-2562.
57. Ezealigo, U. S., Ezealigo, B. N., Aisida, S. O., & Ezema, F. I. (2021). Iron oxide nanoparticles in biological systems: Antibacterial and toxicology perspective. *JCIS Open*, *4*, 100027.

58. Gudkov, S. V., Burmistrov, D. E., Serov, D. A., Rebezov, M. B., Semenova, A. A., & Lisitsyn, A. B. (2021). Do iron oxide nanoparticles have significant antibacterial properties?. *Antibiotics*, *10*(7), 884.
59. Marghussian, V. (2015). *Nano-glass ceramics: processing, properties and applications*. William Andrew.
60. Lin, F. C., & Zink, J. I. (2020). Probing the local nanoscale heating mechanism of a magnetic core in mesoporous silica drug-delivery nanoparticles using fluorescence depolarization. *Journal of the American Chemical Society*, *142*(11), 5212-5220.
61. Brown, S., Santa Maria Jr, J. P., & Walker, S. (2013). Wall teichoic acids of gram-positive bacteria. *Annual review of microbiology*, *67*, 313-336.
62. Conroy, B. S., Grigg, J. C., Kolesnikov, M., Morales, L. D., & Murphy, M. E. (2019). Staphylococcus aureus heme and siderophore-iron acquisition pathways. *Biometals*, *32*, 409-424.
63. Dalgaard, P., Ross, T., Kamperman, L., Neumeyer, K., & McMeekin, T. A. (1994). Estimation of bacterial growth rates from turbidimetric and viable count data. *International journal of food microbiology*, *23*(3-4), 391-404.
64. Sóti, Z., Magill, J., & Dreher, R. (2019). Karlsruhe Nuclide Chart–New 10th edition 2018. *EPJ Nuclear Sciences & Technologies*, *5*, 6.
65. Stetefeld, J., McKenna, S. A., & Patel, T. R. (2016). Dynamic light scattering: a practical guide and applications in biomedical sciences. *Biophysical reviews*, *8*, 409-427.
66. Bunaciu, A. A., UdriŞTioiu, E. G., & Aboul-Enein, H. Y. (2015). X-ray diffraction: instrumentation and applications. *Critical reviews in analytical chemistry*, *45*(4), 289-299.
67. Patterson, A. L. (1939). The Scherrer formula for X-ray particle size determination. *Physical review*, *56*(10), 978.
68. Franken, L. E., Grünewald, K., Boekema, E. J., & Stuart, M. C. (2020). A technical introduction to transmission electron microscopy for soft-matter: Imaging, possibilities, choices, and technical developments. *Small*, *16*(14), 1906198.
69. Orlova, E. V., & Saibil, H. R. (2011). Structural analysis of macromolecular assemblies by electron microscopy. *Chemical reviews*, *111*(12), 7710-7748.
70. Kumar, A., & Dixit, C. K. (2017). Methods for characterization of nanoparticles. In *Advances in nanomedicine for the delivery of therapeutic nucleic acids* (pp. 43-58). Woodhead Publishing.
71. Bhattacharjee, S. (2016). DLS and zeta potential–what they are and what they are not?. *Journal of controlled release*, *235*, 337-351.
72. Wilschefski, S. C., & Baxter, M. R. (2019). Inductively coupled plasma mass spectrometry: introduction to analytical aspects. *The Clinical Biochemist Reviews*, *40*(3), 115.
73. Birks, J. B. (2013). *The theory and practice of scintillation counting: International series of monographs in electronics and instrumentation* (Vol. 27). Elsevier.
74. Schindelin, J., Arganda-Carreras, I., Frise, E., Kaynig, V., Longair, M., Pietzsch, T., ... & Cardona, A. (2012). Fiji: an open-source platform for biological-image analysis. *Nature methods*, *9*(7), 676-682.
75. Singh, A. K., Prakash, P., Achra, A., Singh, G. P., Das, A., & Singh, R. K. (2017). Standardization and classification of in vitro biofilm formation by clinical isolates of Staphylococcus aureus. *Journal of global infectious diseases*, *9*(3), 93.
76. Jones, A. R. (1999). Light scattering for particle characterization. *Progress in Energy and Combustion Science*, *25*(1), 1-53.
77. Swanson, H. E. (1953). *Standard X-ray diffraction powder patterns* (Vol. 25). US Department of Commerce, National Bureau of Standards.
78. Buschow, K. V., Van Engen, P. G., & Jongebreur, R. (1983). Magneto-optical properties of metallic ferromagnetic materials. *Journal of magnetism and magnetic materials*, *38*(1), 1-22.
79. Perversi, G., Cumby, J., Pachoud, E., Wright, J. P., & Attfield, J. P. (2016). The Verwey structure of a natural magnetite. *Chemical Communications*, *52*(27), 4864-4867.
80. Brown, J. R. (1954). The solid solution of cadmium in zinc. *J. Inst. Metals*, *83*.

81. Popović, S. (2020). Quantitative Phase Analysis by X-ray Diffraction—Doping Methods and Applications. *Crystals*, *10*(1), 27.
82. Varenne, F., Coty, J. B., Botton, J., Legrand, F. X., Hillaireau, H., Barratt, G., & Vauthier, C. (2019). Evaluation of zeta potential of nanomaterials by electrophoretic light scattering: Fast field reversal versus Slow field reversal modes. *Talanta*, *205*, 120062.
83. Sun, Q., Cai, X., Li, J., Zheng, M., Chen, Z., & Yu, C. P. (2014). Green synthesis of silver nanoparticles using tea leaf extract and evaluation of their stability and antibacterial activity. *Colloids and surfaces A: Physicochemical and Engineering aspects*, *444*, 226-231.
84. Putra, N. E., Leeflang, M. A., Ducret, V., Patrulea, V., Fratila-Apachitei, L. E., Perron, K., ... & Zadpoor, A. A. (2022). Preventing Antibiotic-Resistant Infections: Additively Manufactured Porous Ti6Al4V Biofunctionalized with Ag and Fe Nanoparticles. *International Journal of Molecular Sciences*, *23*(21), 13239.
85. Kent, R. D., & Vikesland, P. J. (2012). Controlled evaluation of silver nanoparticle dissolution using atomic force microscopy. *Environmental science & technology*, *46*(13), 6977-6984.
86. Trenkenschuh, E., & Friess, W. (2021). Freeze-drying of nanoparticles: How to overcome colloidal instability by formulation and process optimization. *European journal of pharmaceutics and biopharmaceutics*, *165*, 345-360.
87. Sharpe PT. 2012. Methods of Cell Separation. Elsevier Science.
88. Dadfar, S. M., Camozzi, D., Darguzyte, M., Roemhild, K., Varvarà, P., Metselaar, J., ... & Lammers, T. (2020). Size-isolation of superparamagnetic iron oxide nanoparticles improves MRI, MPI and hyperthermia performance. *Journal of nanobiotechnology*, *18*(1), 1-13.
89. Hayden, S. C., Zhao, G., Saha, K., Phillips, R. L., Li, X., Miranda, O. R., ... & Bunz, U. H. (2012). Aggregation and interaction of cationic nanoparticles on bacterial surfaces. *Journal of the American Chemical Society*, *134*(16), 6920-6923.
90. Gouyau, J., Duval, R. E., Boudier, A., & Lamouroux, E. (2021). Investigation of nanoparticle metallic core antibacterial activity: Gold and silver nanoparticles against Escherichia coli and Staphylococcus aureus. *International journal of molecular sciences*, *22*(4), 1905.
91. Kraemer, S. M. (2004). Iron oxide dissolution and solubility in the presence of siderophores. *Aquatic sciences*, *66*, 3-18.
92. Besenhard, M. O., LaGrow, A. P., Hodzic, A., Kriechbaum, M., Panariello, L., Bais, G., ... & Gavriilidis, A. (2020). Co-precipitation synthesis of stable iron oxide nanoparticles with NaOH: New insights and continuous production via flow chemistry. *Chemical Engineering Journal*, *399*, 125740.
93. Sevcenco, A. M., Pinkse, M. W., Wolterbeek, H. T., Verhaert, P. D., Hagen, W. R., & Hagedoorn, P. L. (2011). Exploring the microbial metalloproteome using MIRAGE. *Metallomics*, *3*(12), 1324-1330.

Appendix A

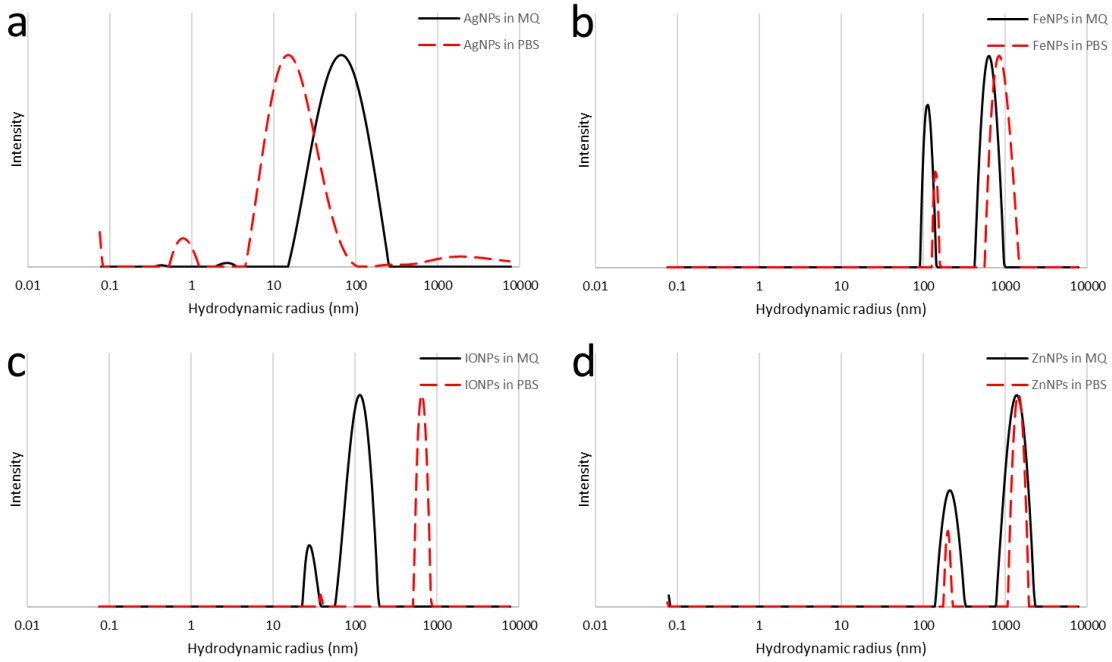

Figure A.1: The size distribution of AgNPs (a), FeNPs (b), IONPs (c) and ZnNPs(d) in MQ (black) and PBS (red).

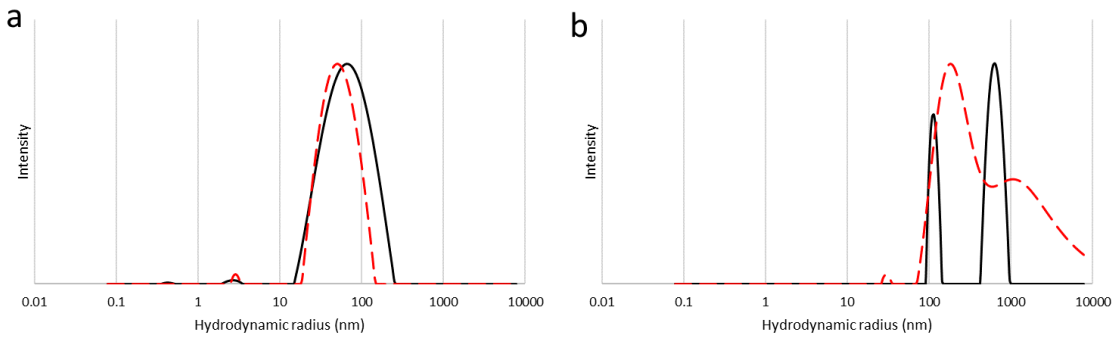

Figure A.2: The size distributions of AgNPs (a) and FeNPs (b) determined with two DLS measurements of the same sample.

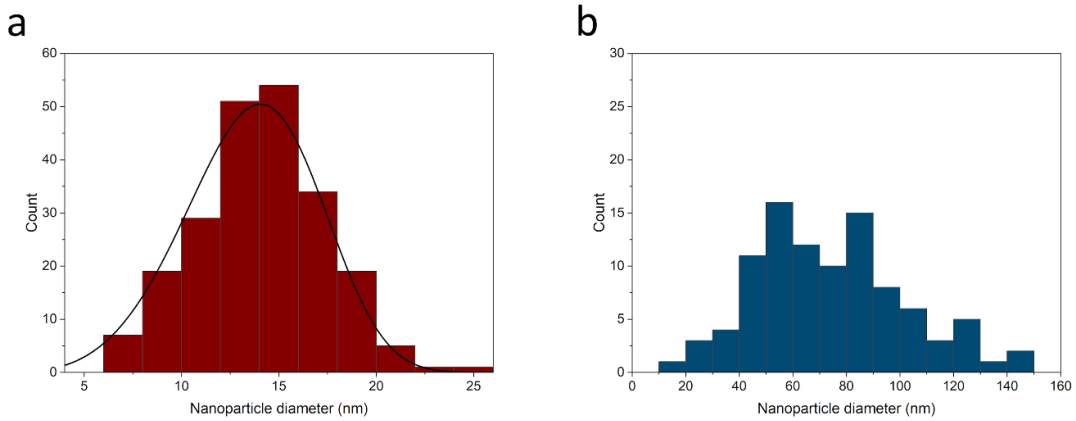

Figure A.3: Histogram of sizes of AgNPs (a) and FeNPs (b) measured with TEM

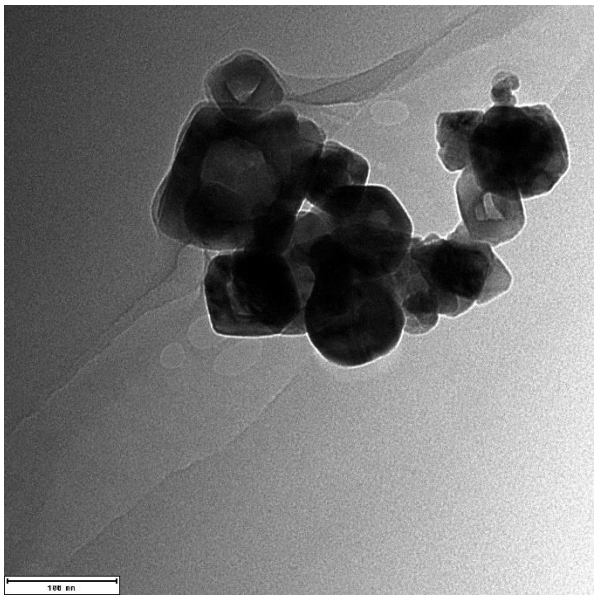

Figure A.4: Non-spherical shapes observed during TEM of iron nanoparticles

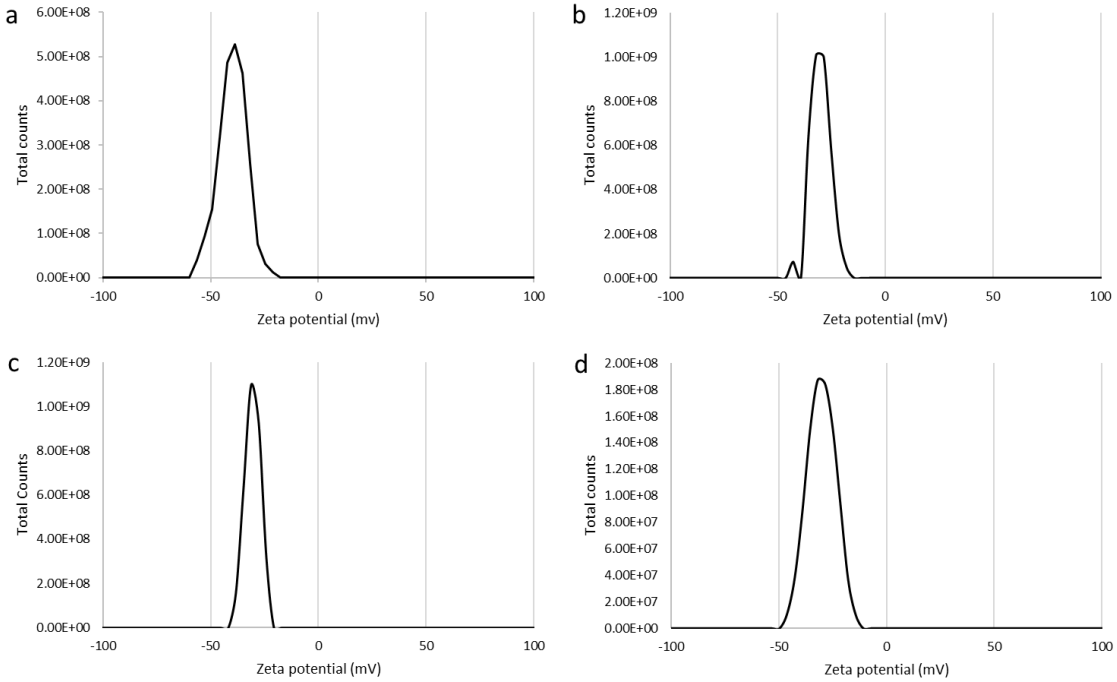

Figure A.5: Zeta potentials of AgNPs (a), FeNPs (b), IONPs (c) and ZnNPs (d).

Tube	Added activity (cpm)	28-day release (wt%)
A	8.21E+05	0.27%
B	8.13E+05	0.28%
C	1.98E+05	1.09%

Table A.1: The activity (in cpm) added to different dialysis tubes, as well as the weight percentage of ions released after 28 days of dialysis

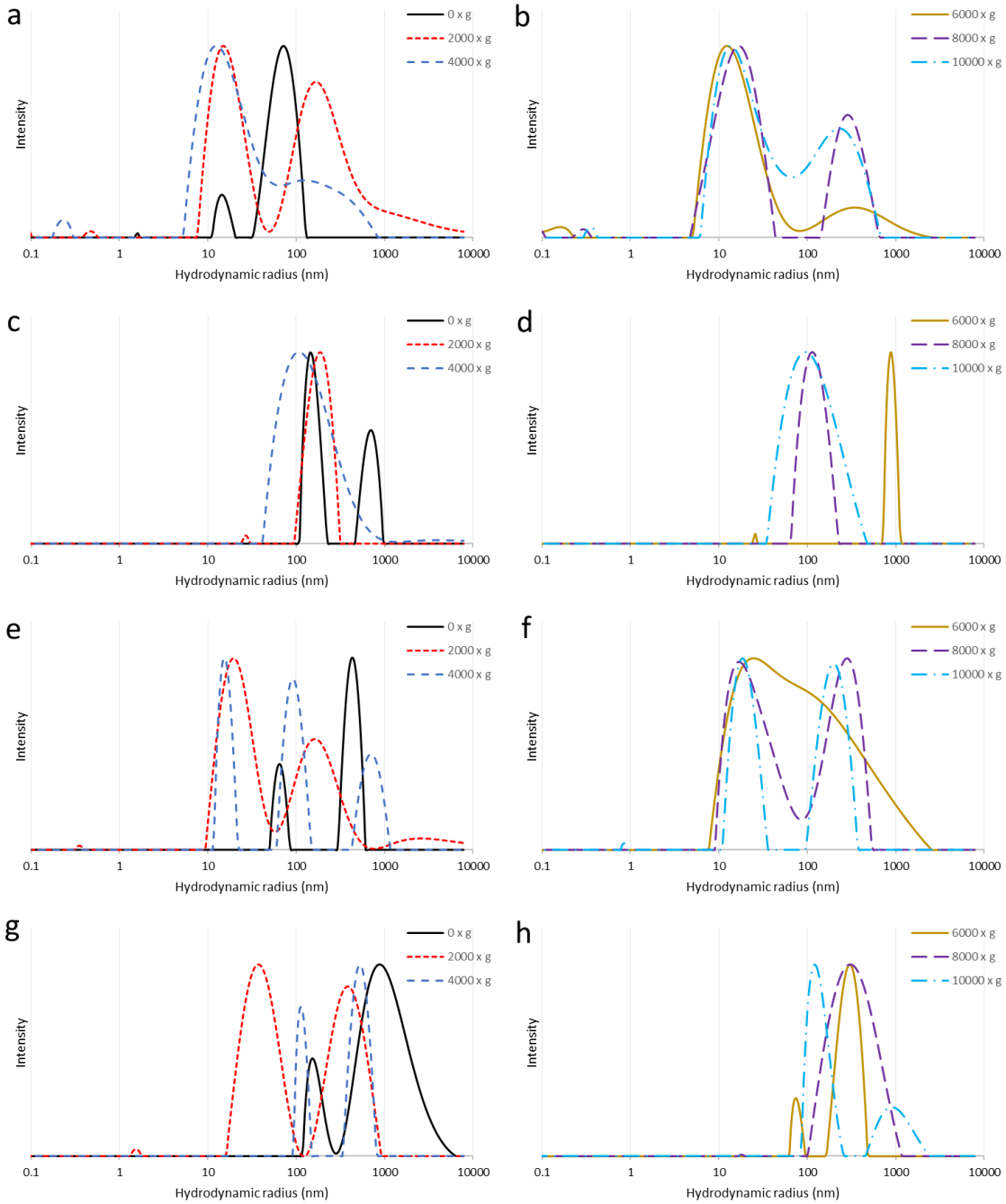

Figure A.6: Size distributions of AgNPs (a,b), FeNPs (c,d), IONPs (e,f) and ZnNPs (g,h) obtained from DLS after centrifuging at various speeds.

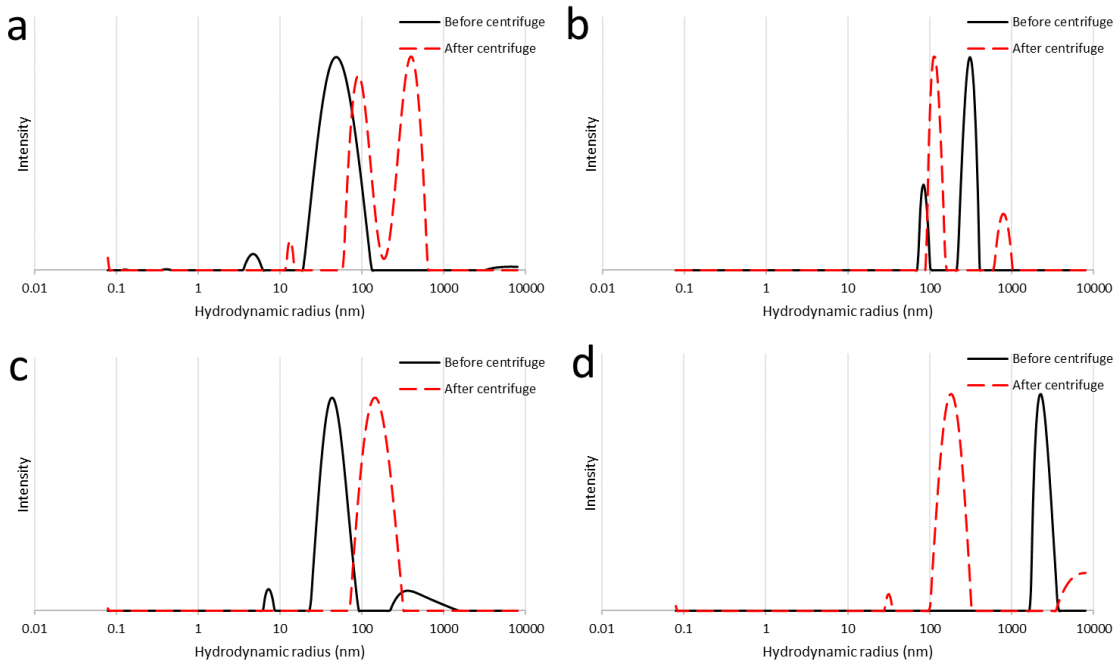

Figure A.7: The size distribution of AgNPs (a), FeNPs (b), IONPs (c), ZnNPs (d) determined with DLS before and after centrifugation at a speed of 100,000 x g, displayed in black and red respectively

Appendix B: Control experiments

B.1: Testing the dialysis membrane

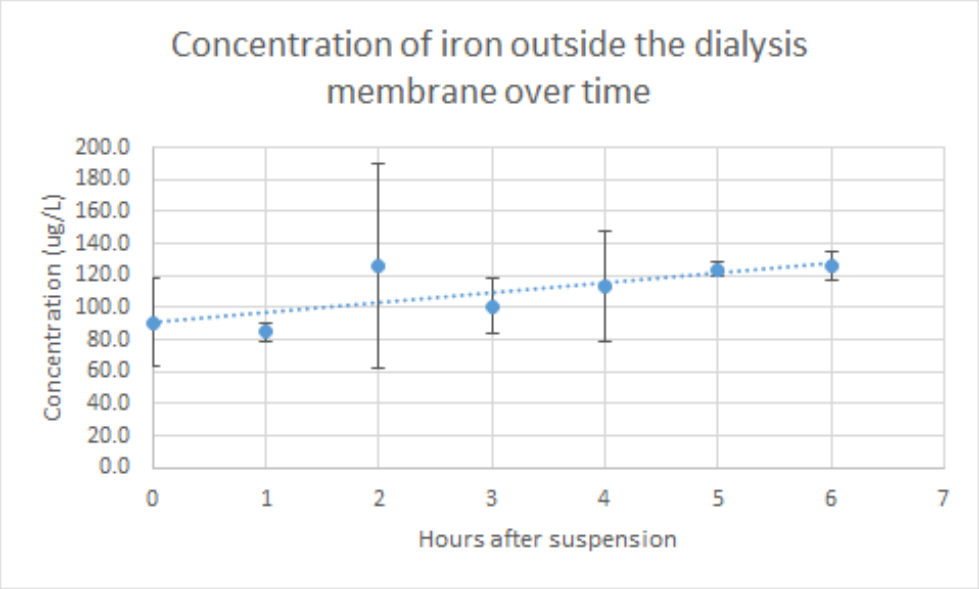

Figure B.1: The concentration of iron outside of a dialysis membrane as determined with ICP-MS

In order to determine whether iron nanoparticles can diffuse through the dialysis membrane used in section 4.1.5, iron nanoparticles were added to a membrane. Every hour, samples were taken of the environment outside the membrane, and the iron content was measured with ICP-MS. It was observed that the concentration of iron increased by 20 µg/ml after 6 hours. These findings, combined with the knowledge that the iron nanoparticles are larger than the pore size of the dialysis membrane, meant that the dialysis membrane could be used for ion release experiments.

B.2: Removal of radioactive nanoparticles

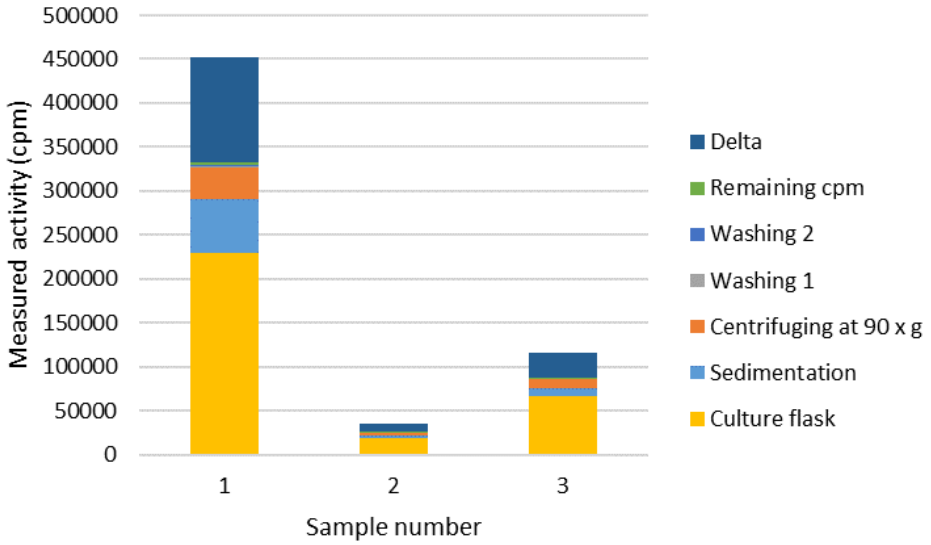

Figure B.1: Activity (in cpm) removed during each stage of the separation protocol.

To test the separation method outlined in section 3.5.3, experiments were performed during which bacteria were grown overnight in a culture flask. After overnight growth, radioactive FeNPs were added. Because the nanoparticles were added after growth had taken place, in combination with the slow ion release rate of FeNPs, it was deemed unlikely for iron uptake to occur. The separation protocol was carried out, and the activity of the waste produced by each stage was measured through the Wallac gamma counter. The measured activities are displayed in figure B.1. ‘Delta’ is calculated by subtracting the obtained activities from the total activity of the added nanoparticles. The relatively high Delta fraction is likely caused by a portion of the nanoparticles remaining attached to the glass of the culture flask. Only 0.5% of activity (and therefore nanoparticles) remained in the sample after the separation protocol.

Appendix C: XRD reference peaks

Presented below are the peaks of the reference XRD data obtained from the ICDD database together with their ICDD codes and reference to the articles they originally came from. Please note that not every reference peak appears in the measured XRD pattern.

Ag reference data (00-004-0783)

No.	h	k	l	d [Å]	2θ [°]	I [%]	
1	1	1	1	2,35900	38,117	100,0	
2	2	0	0	2,04400	44,278	40,0	
3	2	2	0	1,44500	64,427	25,0	
4	3	1	1	1,23100	77,475	26,0	
5	2	2	2	1,17960	81,539	12,0	
6	4	0	0	1,02150	97,891	4,0	
7	3	3	1	0,93750	110,501	15,0	
8	4	2	0	0,91370	114,928	12,0	
9	4	2	2	0,83410	134,889	13,0	

Swanson, H. E. (1953). *Standard X-ray diffraction powder patterns* (Vol. 25). US Department of Commerce, National Bureau of Standards.

Fe reference data (04-003-3884)

No.	h	k	l	d [Å]	2θ [°]	I [%]
1	1	1	0	2,02728	44,663	100,0
2	2	0	0	1,43350	65,008	11,7
3	2	1	1	1,17045	82,314	17,8
4	2	2	0	1,01364	98,917	4,7
5	3	1	0	0,90662	116,344	6,4
6	2	2	2	0,82763	137,097	1,7

Buschow, K. V., Van Engen, P. G., & Jongebreur, R. (1983). Magneto-optical properties of metallic ferromagnetic materials. *Journal of magnetism and magnetic materials*, *38*(1), 1-22.

Fe_3O_4 reference data (04-025-0335)

No.	h	k	l	d [Å]	2θ [°]	I [%]
1	2	0	2	4,83837	18,322	10,2
2	0	2	2	4,83837	18,322	10,2
3	2	2	2	3,74644	23,730	0,1
4	-2	2	2	3,74644	23,730	0,1
5	1	3	2	3,42310	26,009	0,1
6	-1	3	2	3,42310	26,009	0,1
7	-3	1	3	3,12424	28,548	0,1
8	3	1	3	3,11149	28,667	0,1
9	1	1	5	3,11149	28,667	0,1
10	4	0	0	2,97064	30,058	24,4
11	-2	2	4	2,97064	30,058	24,4
12	2	2	4	2,96088	30,159	24,2
13	0	4	0	2,96088	30,159	24,2
14	0	4	1	2,91947	30,597	0,3
15	0	2	5	2,91947	30,597	0,3
16	3	3	0	2,79619	31,981	0,1
17	0	0	6	2,79619	31,981	0,1
18	4	2	0	2,65523	33,729	0,1
19	-3	3	2	2,65523	33,729	0,1
20	2	4	1	2,61868	34,214	0,4
21	-2	4	1	2,61868	34,214	0,4
22	-4	2	2	2,53420	35,391	52,7
23	-2	0	6	2,53420	35,391	52,7
24	4	2	2	2,52813	35,479	100,0
25	0	2	6	2,52813	35,479	100,0
26	-4	0	4	2,42919	36,975	3,4
27	4	0	4	2,41918	37,134	8,8
28	0	4	4	2,41918	37,134	8,8
29	2	4	3	2,39690	37,492	0,2
30	-2	4	3	2,39690	37,492	0,2
31	3	3	4	2,32302	38,731	0,1
32	2	2	6	2,32302	38,731	0,1
33	4	2	4	2,23962	40,234	0,1
34	-1	5	2	2,23962	40,234	0,1
35	0	4	5	2,22172	40,573	0,1
36	0	2	7	2,22172	40,573	0,1
37	-1	5	3	2,14699	42,051	0,1

No.	h	k	l	d [Å]	2θ [°]	I [%]
38	5	1	3	2,14699	42,051	0,1
39	4	4	0	2,09707	43,101	32,0
40	0	0	8	2,09707	43,101	32,0
41	4	4	1	2,08003	43,472	0,5
42	-4	4	1	2,08003	43,472	0,5
43	-5	1	4	2,04063	44,355	0,1
44	-4	0	6	2,04063	44,355	0,1
45	4	0	6	2,03116	44,573	0,2
46	1	5	4	2,03116	44,573	0,2
47	-6	0	2	1,92933	47,064	0,3
48	-4	2	6	1,92933	47,064	0,3
49	6	0	2	1,92555	47,161	0,3
50	-2	4	6	1,92555	47,161	0,3
51	4	2	6	1,92132	47,272	0,5
52	2	4	6	1,92132	47,272	0,5
53	6	2	2	1,83120	49,752	0,1
54	-3	5	4	1,83120	49,752	0,1
55	3	1	8	1,82903	49,815	0,1
56	-2	6	2	1,82903	49,815	0,1
57	1	5	6	1,78629	51,091	0,1
58	0	6	4	1,78629	51,091	0,1
59	2	6	3	1,77568	51,419	0,1
60	-2	6	3	1,77568	51,419	0,1
61	-6	2	4	1,71674	53,320	3,9
62	-4	0	8	1,71674	53,320	3,9
63	4	0	8	1,71109	53,511	7,7
64	6	2	4	1,71109	53,511	7,7
65	5	5	0	1,67771	54,663	0,1
66	0	0	10	1,67771	54,663	0,1
67	-5	1	7	1,67533	54,747	0,1
68	1	7	0	1,67533	54,747	0,1
69	7	1	1	1,67239	54,851	0,1
70	-7	1	1	1,67239	54,851	0,1
71	-1	5	7	1,66897	54,973	0,1
72	-5	5	1	1,66897	54,973	0,1
73	1	7	1	1,66715	55,038	0,1
74	-1	7	1	1,66715	55,038	0,1
75	-7	1	2	1,64896	55,698	0,1
76	-5	3	6	1,64896	55,698	0,1

No.	h	k	l	d [Å]	2θ [°]	I [%]
77	7	1	2	1,64623	55,798	0,1
78	-2	4	8	1,64623	55,798	0,1
79	4	2	8	1,64290	55,921	0,2
80	2	4	8	1,64290	55,921	0,2
81	2	6	5	1,63673	56,151	0,2
82	-4	6	1	1,63673	56,151	0,2
83	6	0	6	1,61420	57,006	24,9
84	0	2	10	1,61420	57,006	24,9
85	-6	4	3	1,58081	58,324	0,2
86	-4	4	7	1,58081	58,324	0,2
87	4	4	7	1,57566	58,533	0,2
88	4	6	3	1,57566	58,533	0,2
89	-5	3	7	1,55574	59,357	0,1
90	6	2	6	1,55574	59,357	0,1
91	-7	3	2	1,53414	60,279	0,1
92	-6	4	4	1,53414	60,279	0,1
93	7	3	2	1,53209	60,368	0,1
94	-4	6	4	1,53209	60,368	0,1
95	-4	2	9	1,52941	60,485	0,1
96	4	6	4	1,52941	60,485	0,1
97	4	2	9	1,52263	60,782	0,1
98	0	6	7	1,52263	60,782	0,1
99	8	0	0	1,48532	62,478	30,2
100	-4	4	8	1,48532	62,478	30,2
101	4	4	8	1,48044	62,707	29,6
102	0	8	0	1,48044	62,707	29,6
103	-8	0	2	1,46368	63,508	0,2
104	-4	0	10	1,46368	63,508	0,2
105	7	3	4	1,45974	63,700	0,2
106	0	4	10	1,45974	63,700	0,2
107	5	3	8	1,45785	63,792	0,1
108	4	0	10	1,45785	63,792	0,1
109	5	1	9	1,45227	64,066	0,1
110	1	5	9	1,45227	64,066	0,1
111	-8	2	2	1,42094	65,654	0,4
112	-4	2	10	1,42094	65,654	0,4
113	8	2	2	1,41857	65,778	0,4
114	-2	4	10	1,41857	65,778	0,4
115	4	2	10	1,41560	65,933	0,6

No.	h	k	l	d [Å]	2θ [°]	I [%]
116	4	6	6	1,41560	65,933	0,6
117	4	4	9	1,39097	67,254	0,1
118	2	8	3	1,39097	67,254	0,1
119	2	0	12	1,36070	68,958	0,1
120	0	2	12	1,36070	68,958	0,1

Perversi, G., Cumby, J., Pachoud, E., Wright, J. P., & Attfield, J. P. (2016). The Verwey structure of a natural magnetite. *Chemical Communications*, *52*(27), 4864-4867.

Zn reference data (01-073-6858)

No.	h	k	l	d [Å]	2θ [°]	I [%]
1	0	0	2	2,47345	36,290	39,6
2	1	0	0	2,30770	38,999	23,7
3	1	0	1	2,09134	43,225	100,0
4	1	0	2	1,68735	54,325	14,6
5	1	0	3	1,34165	70,079	15,9
6	1	1	0	1,33235	70,641	10,3
7	0	0	4	1,23672	77,050	2,4
8	1	1	2	1,17300	82,096	11,1
9	2	0	0	1,15385	83,763	1,3
10	2	0	1	1,12369	86,551	6,8
11	1	0	4	1,09006	89,927	1,9
12	2	0	2	1,04567	94,895	1,6
13	2	0	3	0,94538	109,135	3,2
14	1	0	5	0,90933	115,796	2,9
15	1	1	4	0,90642	116,386	3,8
16	2	1	0	0,87223	124,047	0,8
17	2	1	1	0,85898	127,471	4,8
18	2	0	4	0,84367	131,855	0,8
19	0	0	6	0,82448	138,225	0,5
20	2	1	2	0,82258	138,925	1,5

Brown, J. R. (1954). The solid solution of cadmium in zinc. *J. Inst. Metals*, *83*.

ZnO reference data (00-005-0664)

No.	h	k	l	d [Å]	2θ [°]	I [%]
1	1	0	0	2,81600	31,750	71,0
2	0	0	2	2,60200	34,440	56,0
3	1	0	1	2,47600	36,252	100,0
4	1	0	2	1,91100	47,543	29,0
5	1	1	0	1,62600	56,555	40,0
6	1	0	3	1,47700	62,870	35,0
7	2	0	0	1,40700	66,388	6,0
8	1	1	2	1,37900	67,917	28,0
9	2	0	1	1,35900	69,057	14,0
10	0	0	4	1,30100	72,610	3,0
11	2	0	2	1,23800	76,956	5,0
12	1	0	4	1,18120	81,405	3,0
13	2	0	3	1,09290	89,630	10,0
14	2	1	0	1,06390	92,777	4,0
15	2	1	1	1,04220	95,311	10,0
16	1	1	4	1,01580	98,632	5,0
17	2	1	2	0,98480	102,923	4,0
18	1	0	5	0,97640	104,169	7,0
19	2	0	4	0,95550	107,448	1,0
20	3	0	0	0,93820	110,378	4,0
21	2	1	3	0,90690	116,288	12,0
22	3	0	2	0,88260	121,562	6,0
23	0	0	6	0,86750	125,234	1,0
24	2	0	5	0,83690	133,975	6,0
25	1	0	6	0,82900	136,618	2,0
26	2	1	4	0,82370	138,511	2,0
27	2	2	0	0,81250	142,905	5,0

Swanson, H. E. (1953). *Standard X-ray diffraction powder patterns* (Vol. 25). US Department of Commerce, National Bureau of Standards.